Open Access Dissertations   Electronic Theses and Dissertations

2013-12-17

The Effects of Random Bottom Bathymetry on Coherence in Shallow Water Acoustic Propagation

Jennifer Leigh Wylie
University of Miami, jennie.wylie@gmail.com

Follow this and additional works at: https://scholarlyrepository.miami.edu/oa_dissertations

UNIVERSITY OF MIAMI

THE EFFECTS OF RANDOM BOTTOM BATHYMETRY ON COHERENCE IN
SHALLOW WATER ACOUSTIC PROPAGATION

By

Jennifer Leigh Wylie

A DISSERTATION

Submitted to the Faculty
of the University of Miami
in partial fulfillment of the requirements for
the degree of Doctor of Philosophy

Coral Gables, Florida

December 2013

UNIVERSITY OF MIAMI

A dissertation submitted in partial fulfillment of
the requirements for the degree of
Doctor of Philosophy

THE EFFECTS OF RANDOM BOTTOM BATHYMETRY ON COHERENCE IN
SHALLOW WATER ACOUSTIC PROPAGATION

Jennifer Leigh Wylie

Approved:

_____
Harry A. DeFerrari, Ph.D.
Professor of Applied Marine Physics

_____
Arthur J. Mariano, Ph.D.
Professor of Meteorology &
Physical Oceanography

_____
Jorge F. Willemsen, Ph.D.
Professor of Applied Marine Physics

_____
M. Brian Blake, Ph.D.
Dean of the Graduate School

_____
Kevin B. Smith, Ph.D.
Professor of Physics
Naval Postgraduate School
Monterey, California

WYLIE, JENNIFER LEIGH   (Ph.D., Applied Marine Physics)

<u>The Effects of Random Bottom Bathymetry</u>   (December 2013)
<u>on Coherence in Shallow Water Acoustic</u>
<u>Propagation</u>

Abstract of a dissertation at the University of Miami.

Thesis supervised by Professor Harry A. DeFerrari.
No. of pages in text. (73)

In an ideal shallow water propagation channel the sound field is accurately described by normal modes and the mode structure is predictable with clean separated modes. However the real ocean environment is rarely ideal, and variations in bottom bathymetry and water column sound speed are usually present. Random fluctuations of the sound speed in time, space, and/or the boundaries can distort modes such that phase coherence is reduced and under some conditions completely lost.

The basic research community seeks to understand the effects of internal waves on temporal coherence. Here the study method of choice is to use fixed system experiments that observe both oceanographic and acoustical fluctuations. On the other hand applied Naval research is focused on using mobile platforms to instantaneously measure spatial coherence shipboard, and they have little to no interest in measuring long term coherence.

Here we seek to present a unified theory using normal modes. Both spatial and temporal coherence as well as the effects of source motion and Doppler will be addressed. Mode structure can be randomized in two ways: sound speed fluctuations and boundary variations. The research proposed here will emphasize spatial variations of the

bottom bathymetry and how they affect mode arrivals. A parabolic equation model is used to predict mode shapes in a range dependent environment and random variations in bottom boundaries will be introduced and distortion in the mode arrival structure will be observed. The mode arrival structures will then be used to estimate temporal and spatial coherence of the mode arrivals and the predictions will be compared to the data from three different shallow water experiments.

TABLE OF CONTENTS

Page

List of Figures

Chapter 1
Introduction

Much previous research has been focused on the mechanisms that lead to the loss of acoustic coherence in the ocean[1,2,3]. Coherence is of utmost importance in ocean acoustics research because it implies phase and/or amplitude stability of a signal in space/time. All signal processing methods use this stability to achieve gain or signal enhancement above the incoherent background noise. Without coherence, signals resemble the noise background and therefore there can be no signal processing gain.

Just like transmission loss, coherence is a measurable and sometimes predictable characteristic of the propagation channel. Variability of the sound speed along the path of propagation, caused by oceanographic variability, reduces the coherence of propagating signals. Likewise fluctuation of the channel boundaries, surface and bottom, can reduce coherence in space and also time when combined with source/receiver motion.

Early studies of coherence, commenced in the late 1960's and continued through the 1990's, were mostly concerned with deep ocean low-frequency propagation[4,5]. Motivation was to support the Navy submarine surveillance system, SOSSUS. SOSSUS listening stations were worldwide and sought to detect and track Russian submarines. They relied on "tonals" generated by the submarine vibrations. The tonals were signal frequency, continuous wave, or CW-like, and the ocean was found to be so stable that 20 to 30 dB of phase coherent signal processing gain was routinely observed.

The limiting factor on signal coherence was caused by oceanographic fluctuations - namely ubiquitous internal gravity waves. Irregular ocean boundaries usually had

negligible effect in typical deep ocean environments. So the research concentrated on the effects of internal waves on CW multipath transmission.

The demise of the Soviet Union and the end of the Cold War coincided with a shift of Navy research emphasis from the deep ocean to the shallow seas. The approach taken for the shallow water research was mostly a continuation of the deep water methods used previously and continued to consider multipath coherence caused by internal waves. However shallow water propagation differs from the deep ocean in fundamental ways; multiple interactions with bottom/surface boundaries are the rule rather than the exception and shallow water internal waves have distinctly different features than those propagating in the deep ocean. Further, studying the combined multipath signal obscures the basic physics at play owing to the fact that each mode has different interaction angles.

More recent works have tried to make strides in understanding coherence using mode-coupling theory. Works by McDaniel and McCammon[6] and Preisig and Duda[7] and Duda and Preisig[8] examined the effects of bottom variability and internal wave variations on mode coherence. However, in each of the works, the other contributing factor was held constant and recent experimental observations have indication that both need to be taken into account to fully understand coherence.

Temporal coherence has been studied at several shallow water sites around the world[1,2]. Three of these are of particular interest to this effort; 1) the Shallow Water 2006 Experiment (SW06), 2) Acoustic Observatory Calops Experiments (AOCE), and 3) The Florida Straits Propagation Experiments (FSPE). All three of these have consistent and comparable signal types and processing, and all were designed to

have separable and resolvable mode arrivals so that coherence can be measured for individual modes of propagation. Several octaves of frequency were used for all three sites and some horizontal line array (HLA) and vertical line array (VLA) data were taken. These data provide observations of both the singular mode and mode combined coherencies over a broad range of frequencies and for a wide variety of oceanographic conditions, such as internal wave types, and for different ranges depths and bottom properties.

Some results of analysis of these data sets show remarkable consistencies amongst sites and for differing channel parameters. Clean stable modes always result in coherent transmission in both time and space. Lower order modes are always more coherent than higher order modes. Also, as identifiable mode structures deteriorate so does coherence. A working hypothesis of this thesis is that understanding the physics of mode stability and the physics of coherence are one and the same. Without stable mode formation in shallow water one cannot observe coherence.

In this work the coherence and mode structure data from the three aforementioned shallow water sites will be reanalyzed. In addition, the Monterey Miami Parabolic Equation (MMPE) propagation model[9] will be used to further explain these results. By using MMPE to systematically analyzing each individual variable that plays a role in shallow water propagation, we hope to gain a better understanding of the whole system. First a random bottom will be introduced into the propagation model in order to develop a statistical representation of the effect of bottom fluctuations on mode arrival structure. Finally, sound speed column variability is introduced into the model and temporal coherence is computed over the average internal wave period.

The relationship between source motion and coherence lengths are also investigated. In particular, at what speed of the source relative to a stationary receiver does the source motion become a primary factor in coherence loss.

1.1 Background Theory

Ray Theory

Some of the earlier methods of understanding the impact of the environment on the acoustic field involved ray theory and ray tracing. In a notable example involving the Straits of Florida, Palmer[10] found that ray paths become chaotic in the presence of small scale bathymetric variations and distinct rays cannot be identified after several bounces. He then used ray theory in an attempt to study the sensitivity of the acoustic field to small scale ocean structure[11]. A linear sound speed profile was used and the bathymetry was modeled as a sum of the large scale ocean bathymetry $b_{avg}(r)$ and a small scale bottom structure $\delta b(r)$

$$b(r) = b_{avg}(r) + \delta b(r). \tag{1.1}$$

The small scale bathymetric function used was a summation of harmonics with amplitude on order of 10cm and wavelengths between 300-500m,

$$\delta b(r) = A \sum_{i=1}^{10} cos[2\pi(\frac{r}{\lambda_i} + \phi_i)]. \tag{1.2}$$

Palmer found that when small scale structure was present, the eigenrays (the rays that

begin at the source and end at the receiver) become broken up into micromultipaths such that what existed as only one eigenray when $\delta b(r) = 0$ became multiple eigenrays when $\delta b(r)$ is non-zero. This introduces an uncertainty or blurring into the ray path, and that blurring can result in a loss of spatial resolution and horizontal coherence. This was interpreted by Palmer to be classical chaos. The question arises as to weather such chaos is observable in the data or just in the non-linear equations of the ray approximation.

However, as the acoustic community has moved from using ray solutions to full wave solutions it was found that the introduction of classical chaos does not impact the full wave predictions of coherence results in such environments. Additionally, experimental observations, including those in the Straits of Florida, have show that in the real ocean environment, clean separable modes (which can be thought of as a combination of up and down going plane waves) are present and can remain coherent in both time and space, and indeed classical chaos is only manifested in the non-linear ray equations and the not the full-wave propagation measured in the real ocean.

Mode Coupling Theory

Mode coupling is the transfer of energy between acoustic modes. Many different studies have been conducted on mode coupling, however the interest here is coupling of modes due to internal wave activity. There have been several different theoretical studies on the coupling of modes, but here the methods of Creamer[12] will be followed.

Assume that the sound speed is

$$c(r, z, t) = c_0(z) + \delta c(r, z, t); \tag{1.3}$$

where c_o is the deterministic sound speed profile and δc is a correction to the background profile that is modeled as a stochastic process. Then the time and range independent part of the complex acoustic wavenumber becomes

$$\tilde{k}_A(z) = \frac{\omega}{c_o(z)} + i\alpha(z). \tag{1.4}$$

The modal decomposition to the Helmholtz equation becomes,

$$p(r, z) = \sum_{n=1}^{N} \frac{A_n(r)}{\sqrt{k_n r}} \phi_n(z). \tag{1.5}$$

$A_n(r)$ is the nth range dependent modal amplitude. This modal decomposition is an orthonormal set of basis functions with each mode carrying a part of the total energy. It is analogous to a set of "vibrating strings." The normal modes satisfy the equation,

$$\frac{d^2\phi_n(z)}{dz^2} + \tilde{k}^2(z)\phi_n(z) = l_n^2\phi_n(z). \tag{1.6}$$

Using the quasi-static, narrow angle, weak scattering approximation[13, 14] the modal amplitudes will obey,

$$\frac{\partial A_n}{\partial r} - il_n A_n = -i\sum_{m=1}^{N} \rho_{nm}(r, t) A_m. \tag{1.7}$$

l_n is the complex horizontal wavenumber defined by

$$l_n = k_n + i\alpha_n \tag{1.8}$$

and α_n is the modal attenuation,

$$\alpha_n = \frac{\omega}{k_n} \int dz \frac{\alpha(z)}{c_o(z)} \phi_n^2(z). \tag{1.9}$$

Finally, the mode coupling term ρ_{nm} is defined in terms of the stochastic random sound speed perturbations by,

$$\rho_{nm} = \frac{k^2}{\sqrt{k_n k_m}} \int dz \frac{\delta c(r,z,t)}{c_o} \phi_n(z)\phi_m(z). \tag{1.10}$$

Here the focus will be on solitary internal waves with focus on the New Jersey shelf area, where the waves occur with regularity and are highly nonlinear. Mode coupling through internal waves depends on may factors: internal solitary wave amplitude, width, depth structure, location to the source and direction of propagation relative to the acoustic path of interest. The majority of studies have focused on internal wave propagation parallel to the path of acoustic propagation and at low frequencies ($< 400 Hz$).

Presig and Duda[7] found that the net effect to the total individual mode energy due to coupling is highly scale dependent. The modeling was done with only one internal wave. There is strong coupling within the internal solitary wave from lower modes to higher modes for internal waves with a width scale of less than 75m. However,

an "uncoupling" occurs when the acoustic field exits the trailing edge of the internal wave and that there is, in effect, no net coupling in these regimes. At medium scales ($75 - 200m$) there is both coupling and transparent resonance (where the ISW field appears transparent to the acoustic modes), with the relative phase of the modes being the dominating factor. Finally at higher order scales (greater than 200m), there is primarily transparent resonance with the propagation appearing to be adiabatic. Presig and Duda[8] found that the relative position of the internal wave packet to the acoustic source also impacts the coupling. If the wave packet is close to the acoustic source the energy is transferred from higher order to lower order modes and if the wave packet is far from the source the energy couples from lower order to higher order modes.

Young[15] investigated three wave packets and found mode coupling is dominated by the first wave in a packet. Colosi[16] modeled internal wave propagation perpendicular to the acoustic path. He found that mode coupling is impacted by modal attenuation, where at low frequencies the attenuation broadens the number of resonances in wavenumber which allows for a greater number of non-linear internal wave components to interact with the acoustic modes.

Rouseff[17] examined the temporal coherence of acoustic modes propagating through internal waves with interest being paid to results from the Shallow Water Acoustics in Random Media (SWARM - 95) experiment. The experiment was conducted off the New Jersey shelf with similar internal waves types as those in the Shallow Water 2006 (SW06) experiment. It was predicted that a decorrelation of modal amplitude due to mode coupling during propagation through a solitary internal wave would be on the

order of approximately $100s$. However a recoupling is shown at larger time scales. At higher frequencies (400Hz) modal amplitudes decorrelate quicker than lower frequencies (224Hz). At 400Hz the modal amplitude variation of the acoustic field has rich structure, while at 224Hz the modal amplitudes demonstrate a more slowly varying structure. However it must be noted that the calculation of temporal coherence here did not seem to take phase dependence into effect, and that the results may have longer coherence times.

In addition to mode coupling from internal wave fluctuations, mode coupling from bottom interaction has been previously studied. The formulation from McDaniel[6] will be followed. Two different mode coupling cases were studied: weak coupling with a bottom slope of approximately $0.5°$ and strong coupling with a bottom slope of approximately $5.7°$. Fluctuations of the sound field in the water column were ignored and a smooth velocity profile was used. Williams[18] had previously found that coupling between modes was significant if the dimensionless parameter

$$\gamma = \frac{fH}{c_1} \sim 10, \tag{1.11}$$

where f is the source frequency, H is the water column depth, and c_1 is the sound speed of the isovelocity layer. It was found that the coupling coefficient between two modes for a smooth ocean bottom with slope slowly varying in range is

$$C_{nm} = -2\rho_1(k_n^2 - k_m^2)^{-1}\frac{dh}{dr}[Z_{m1}Z_{n1}(\gamma_{m1}^2 - \frac{\rho_1}{\rho_2}\gamma_{m2}^2) + \frac{\partial Z_{m1}}{\partial Z}\frac{\partial Z_{n1}}{\partial Z}(1 - \frac{\rho_2}{\rho_1})]. \tag{1.12}$$

Z_n is a superposition of the up and down traveling plane waves,

$$Z_{n1} = A_n exp[i\gamma_{n1}(z+h)] + B_n exp[-i\gamma_{n1}(z+h)], \qquad (1.13)$$

$$\gamma_{n1}^2 = K_1^2 - k_n^2, \qquad (1.14)$$

and

$$\gamma_{n2}^2 = K_2^- k_n^2. \qquad (1.15)$$

K_1 and K_2 are propagation constants associated with the water and sediment layers at the interface.

In the case of weak coupling with only the first mode excited it was found that the magnitude of higher order modes will be periodic with range. By examining the amplitude of higher order modes to the initial amplitude of the first mode, which is a measure of the energy exchanged between modes, it is found that the importance of coupling increases with frequency and for large values of γ significant coupling can occur between neighboring modes. Finally the weak coupling solution was found to be in good agreement with a parabolic equation model.

In the strong coupling case examined, chosen such that the third mode contains virtually all the energy at range, it is found the if the receiver is located at the node of the third mode, there is significant coupling and a 15dB disagreement between coupling theory and adiabatic normal mode theory. Coupling theory and adiabatic normal mode theory are in good agreement with each other if the receiver is not located on the node of the third mode.

The effects of both solitary internal waves (SIW's) and bathymetric fluctuations on mode coherence will be investigated in this dissertation. Mode coupling effects will not be directly examined as it is cumbersome to the problem. The concern is not the source of the scattered energy but rather the total randomizing effect. However, the MMPE model has sufficient resolution such that if coupling effects occur, they will be part of the modal arrival structure output used in the coherence calculations.

Surface Scattering

In addition to bottom bathymetry and water column sound field fluctuations, the acoustic field makes multiple interactions with the ocean surface. Here previous works on scattering from the ocean surface will be examined and a discussion upon why contributions from the ocean surface can be ignored at the low frequencies of interest to this paper.

The well known Lloyd's mirror effect occurs when sound generated from an acoustic source is reflected from a smooth surface and a well known and much studied interference pattern forms between the direct path and reflected path at the receiver. However, when incident upon a rough and moving surface the acoustic energy becomes scattered and the interference pattern more finely structured.

It is generally accepted that signals reflected from a time varying ocean surface become modulated in both amplitude and phase. Furthermore, the signal is reflected in such a way that its frequency components become smeared about the carrier frequency with evenly formed side-lobes[19].

Some of the early well known work on surface scattering was completed by Rod-

erick and Cron[20]. They studied the frequency spectra of forward scattered sound from the ocean surface. They developed a single frequency theory and obtained the following solution for the normalized scattered pressure in and close to the specular direction:

$$p(A) = \sum_{-\infty}^{\infty} J_n(ckh) \frac{sin(ak - nK)L}{(ak - nK)L} cos[(\omega - n\omega_s)t - \frac{n\pi}{2}].$$ (1.16)

Here J_n is a Bessel function of the fist kind of order n, a and c are the sum of the directional cosines with the x and z axes respectively, k is the acoustic wavenumber, K is the surface wavenumber, h is the wave height, and $2L$ is the length of the surface ensonfied in the direction of the surface wave propagation.

In general, the previous equation leads to the following information about the scattered field: new frequency components are generated, the amplitude of the scattered order is dependent on the corresponding nth order Bessel function, and the acoustic signal is scattered in directions determined by

$$sin\phi_n = sin\theta - \frac{nK}{k}.$$ (1.17)

In addition the carrier frequency is always reflected specularly and the side bands are symmetrically positioned about the carrier and displaced from the carrier at multiples of the surface frequency.

Two different experiments were conducted: an ocean experiment and a tank experiment. The tank experiment was conducted at 225Hz with smaller scale scattering done from controlled sinusoidal waves. The ocean experiment was conducted at two

frequencies, 750Hz and 1500Hz, and source/receiver geometry was set in a way such that the received signals were reflected from the surface at a 7° grazing angle.

The tank experiment found that increases in wave height produced more higher order sidebands. The ocean experiment confirmed this; basically, that as sea state increases more energy is found in the sidebands, and as acoustic frequency is increased more energy is found in the sidebands. With a 35kt wind the carrier frequency is still above the side bands at 750Hz. However, at 1500Hz the carrier frequency is suppressed and almost all energy is contained in the scattered frequency components.

Parkins[21] looked at scattering from two different cases: a slightly rough sea surface and a very rough sea surface. The results from the slightly rough sea surface were as expected and followed the same patterns as shown by Roderick and Cron. The scattering from the very rough sea surface was found to be a very diffuse scattering which causes the spectral line to broaden into a Gaussian curve which shifts and changes in width with sea state, angles of incidence, and source/receiver geometry.

Mitchell and Machell[22] completed an ocean experiment in 1650m of water and with a 250-650Hz broadband source. Here the grazing angles were between $23 - 73°$ and the source was towed at a depth of 60m from a range of 4km to 550m. They had a nondirectional projector and the received signals were a superposition of components dominated by the direct and surface reflected path. They found that at lower frequency and low grazing angles the amplitudes of the spectral modulations were the greatest, which meant there was lower loss. The modulation was not a fixed function of range; therefore surface reflected loss was not a fixed function of surface reflection angle. Finally, the averaged surface reflection loss follows a general

dependence with angle and frequency.

The last article discussed on surface scatting is by Brown and Frisk[23]. They completed ocean experiments in the 100Hz-500Hz range. They experimentally found results consistent with the theory that the acoustic scattering is directly related to the surface wave spectrum through a response function that depends on both the acoustic carrier and surface wave frequencies. They theorized that the acoustic power takes the form:

$$A(\omega) = B(\omega)S(\omega), \tag{1.18}$$

where $S(\omega)$ is the surface wave power spectrum and $B(\omega)$ is the frequency response function of the acoustic signal to the sea surface. Then with small roughness and equal source/receiver depths $B(\omega)$ takes the form,

$$B(\omega) = k^2|F|^2cos^2\theta, \tag{1.19}$$

with F being the Fourier transform of the ensonification function, k the acoustic wavelength and θ the specular angle with respect to the normal surface.

More recent studies have been conducted on surface scattering; however, they primarily involved using the techniques presented here to do an oceanographic study of surface waves and prediction of sea state.

Surface scattering from moving ocean surface waves can cause signal variability with the reflected signal modulated in both amplitude and phase, but there is always a specular reflection at exactly the carrier frequency. Furthermore, the signal is reflected in such a way that its frequency components become Doppler smeared about

the carrier frequency with evenly formed side-lobes and these contributions can be removed by a narrow band filter. As long as the carrier frequency does not become suppressed and the side lobe reflections are filtered, there is no impact from the surface on the temporal coherence of the signal at a submersed hydrophone. Results published by Roderick and Deavenport[24] support that below 1000Hz, a wind speed above 25kts is needed in order to suppress the carrier frequency. From these results, the surface contribution will be ignored in this dissertation.

Normal Mode Theory

The Monterey-Miami Parabolic Equation (MMPE) model[9] was chosen for the analysis. Parabolic equation models are traditionally the model of choice for range dependent problems. The other two readily available model choices, normal mode and ray tracing, were determined not to be good candidates for the modeling needs presented. Normal mode models are generally not used for complicated range dependent problems, as they tend to be more computationally intensive than PE models. Ray tracing models are too unstable and coarse. In addition, ray-tracing models are best used in situations where the acoustic wavelength is small compared to the physical scales. While useful in deep water and higher frequencies, the scales addressed in this work result in bathymetric changes on the same order as the acoustic wavelength[25].

The MMPE computational algorithm is is based on a fast Fourier transform method to solve the parabolic wave equation. Instead of reproducing the well documented method of solving the parabolic equation here the, there are very good readily available descriptions available[9, 26, 27, 28].

A paper by Smith and Smith[28] attempts to clarify the relationship between the wide angle approximation to the parabolic wave equation and the normal mode solution to the elliptic wave equation. Beginning with the Helmholtz equation in cylindrical coordinates

$$\frac{\partial^2 p}{\partial r^2} + \frac{1}{r}\frac{\partial p}{\partial r} + \frac{\partial^2 p}{\partial z^2} + k_o^2 n^2 p = 0, \tag{1.20}$$

they then assume a separation of variables solution of the form

$$p(r,z) = \phi(r)\psi(z). \tag{1.21}$$

Plugging in the assumed solution to the wave equation gives the depth dependent modal wave equation,

$$\frac{\partial^2}{\partial z^2}\psi_m(z) + [k_o^2 n^2(z) - k_m^2]\psi_m(z) = 0, \tag{1.22}$$

where k_m^2 is the separation constant (mode wave number squared) and $\psi_m(z)$ is the depth dependent mode function for that separation constant. Then the entire pressure field can be represented by a summation of all normal modes,

$$p(r,z) = \sum_{m=1}^{\infty} \phi_m(r)\psi_m(z) \tag{1.23}$$

with

$$\phi_m = H_o^1(k_m r). \tag{1.24}$$

The depth dependent modal equation then can be written in the operator notation

$$q\psi_m(z) = \lambda_m \psi_m(z). \tag{1.25}$$

This notation is an eigenvalue equation with operator q and eigenvalues given by

$$\lambda_m = \frac{k_m^2 - k_0^2}{k_0^2}. \tag{1.26}$$

In Smith and Smith[28] the authors assume the function $\phi(r, z)$ to be given by

$$\phi(r, z) = \sum_{m=1}^{\infty} \Gamma_m(r)\nu_m(z). \tag{1.27}$$

Here $\Gamma_m(r)$ is the wide angle parabolic equation range dependent modal amplitude and $\nu_m(r)$ is the wide angle parabolic equation mode function. This assumption and the application of the wide angle propagator function lead to the modal equation

$$\frac{ik_o}{\nu_m(z)}[(1 + \frac{1}{k_o^2}\frac{d^2}{dz^2})^{\frac{1}{2}} + (n(z) - 1)]\nu_m(z) - \frac{1}{\Gamma_m(r)}\frac{d}{dr}\Gamma_m(r) = 0. \tag{1.28}$$

Defining the separation constant as $i\beta(m)$ then

$$\Gamma_m(r) = b_m e^{(i\beta_m r)}. \tag{1.29}$$

Here b_m is the range independent modal amplitude and β_m is the associated wide angle parabolic equation modal wave number. Using this approximation, the modal

equation then becomes to first-order

$$[(1 + \frac{1}{k_0^2}\frac{d^2}{dz^2})^{\frac{1}{2}} + (n(z) - 1) - (1 + \frac{\beta_m}{k_o^2})]\nu_m(z) = 0, \tag{1.30}$$

and to 2nd order

$$[\frac{1}{8k_0^4}\frac{d^4}{dz^4} - \frac{1}{2k_0^2}\frac{d^2}{dz^2} - n(z) - \frac{\beta_m'}{k_o}]\nu_m(z) = 0. \tag{1.31}$$

After applying numerical techniques which will not be reproduced here for brevity reasons, the modal amplitudes are found to be,

$$A_m(r) = \sqrt{(r)}\int_0^D \frac{p(z,r)\nu_m(z)}{\rho(z)}dz. \tag{1.32}$$

Typical modal eigenvalues had less than a 0.03% disagreement from standard normal mode theory and for all modes considered. Modal amplitude calculation had more variation than standard normal mode theory but there was good agreement for mode numbers less than mode 15 for the 1st order approximation and mode number 35 for the 2nd order approximation. Their results confirmed that the wide angle approximation utilized in the MMPE model produces sufficiently accurate solutions to the model structure of the propagating acoustic field.

1.2 Motivation

The three sites analyzed for this work are the site of the SW06 experiment located on the NJ Shelf and the site of the AOCE and FSPE in the Straits of Florida. All
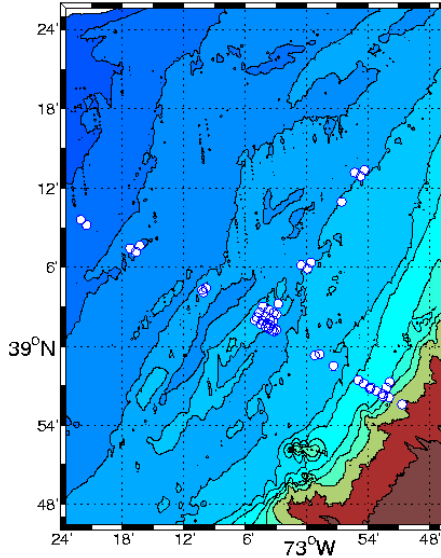
Figure 1.1: : Bathymetry of the SW06 site. Contours at 40, 50, 60, 70, 100, 120,150 200, 500, 1000 meters. Reprinted from Woods Hole Oceanog. Inst. Tech. Rept., WHOI-2007-04.

sites are characterized by relatively flat bathymetry located next to the shelf break. The NJ shelf site is shown in Figure 1.1 with the experiments traversing along the shelf on the 80 m contour. While much of the experiment site may be described as gently sloping across shelf, localized bathymetry variations of 7-8m over several km are feasible along the acoustic path[29]. The SW06 Site in particular is characterized by regular periods of internal wave activity. Internal wave activity is generated by the spilling of tidal current over the shelf edge, resulting in internal waves that are periodic and timed with the tides (DeFerrari, 2008). The experimental sources were designed to have enough bandwidth to separate surface-reflected/bottom-reflected (SRBR) modal arrivals in time. There was no need for mode decomposition.

The bathymetry of the AOCE and FSPE site is illustrated in Figure 1.2. The array used for the AOCE analysis is located along the Miami terrace, an area of
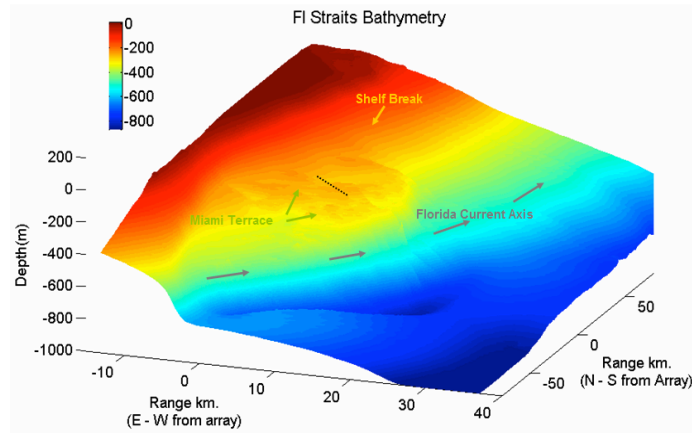
Figure 1.2: Bathymetry of the Florida Straits

relatively flat bathymetry at a depth of about 250m. This site differs from the SW06

site in the type of internal wave activity. The SW06 site is a retrograde front, wherein

the currents block IW activity from the ocean from propagating up the shelf so the

only source of internal waves is the tidal activity. The Florida Straits site is located

along a prograde front. Here the IW activity from the open ocean is able to propagate

along the shelf resulting in an area more saturated in internal wave activity

The data of interest here is from the Shallow Water 2006 (SW06) experiment, with

the Miami Sound Machine (MSM) as the acoustic source and the receivers were single

hydrophone receiver units. The m-sequence data is at frequencies of 100Hz, 200Hz,

800Hz, and 1600Hz and the frequency transmission was switched every 2 hours. The

data has negligible source motion making it ideal for coherence calculations, and the

2hr transmission times allow for coherence calculations up to 1 hour.

Assuming a specular reflection from the ocean surface, the only possible causes

of mode distortion are due to bottom interactions[30, 31] and interactions with internal

wave fields[8,7]. In order to distinguish between coherence losses from both of these causes, the coherence was calculated at periods of high and low internal wave activity. The potential energy (PE) of the internal wave field can be estimated from the temperature data using equation[32]

$$PE = \frac{\rho}{2}\eta^2 N^2,$$ (1.33)

where N is the buoyancy frequency and

$$\eta = \frac{T'}{\frac{dT}{dz}}.$$ (1.34)

The temperature field and the resultant potential energy field are shown in Figure 1.3. Periods of higher and lower internal wave activity are clearly distinguishable

During times of both low and high internal wave activity, the mode structure of the 100Hz data remains stable and the modes remain coherent over the 60-minute calculation period (Figure 1.4). However, the low IW activity coherence undergoes a phase shift due to the barotropic tide. Due to the stability of the mode structure, the 100Hz field appears to be interacting with neither the IW field nor the bottom, meaning the bottom appears essentially flat to the acoustic field.

Effects from bottom interactions and IW activity become apparent when analyzing the 200Hz data, which is presented in Figure 1.5 for periods of both high and low IW activity. During the period of low internal wave activity the mode structure remains stable and the first mode remains coherent. However, the later modes
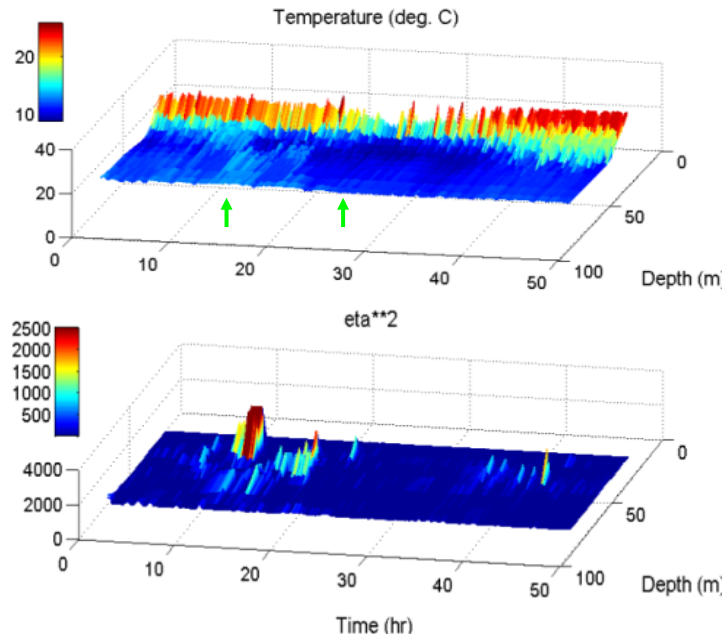
Figure 1.3: The temperature data during the SW06 experiment (top), the two arrows point to periods of high and low internal wave activity. η^2, which is proportional to the potential energy of the internal wave field (bottom).

begin to decrease in coherence exponentially. Without IW activity, scattering due to bottom interactions is the likely cause of coherence loss. The later modes have greater interactions with the bottom, from either number of interactions or angle of incidence, resulting in the loss of coherence. The modes begin to lose stability during the period of higher IW activity and only the first mode remains coherent. Naturally, the modes are still interacting with the bottom during this time period. However, in this case, the internal wave activity has become the dominant contributor in the loss of coherence.

The 800Hz data (Figure 1.6) presents only a stable and coherent first mode in the low IW case, and no stability in the high IW case. Examining just the low IW
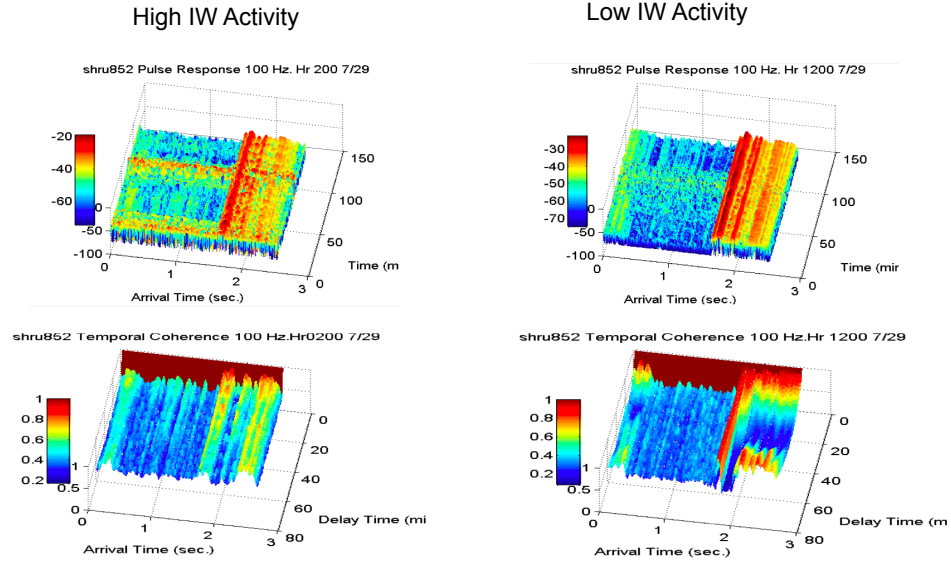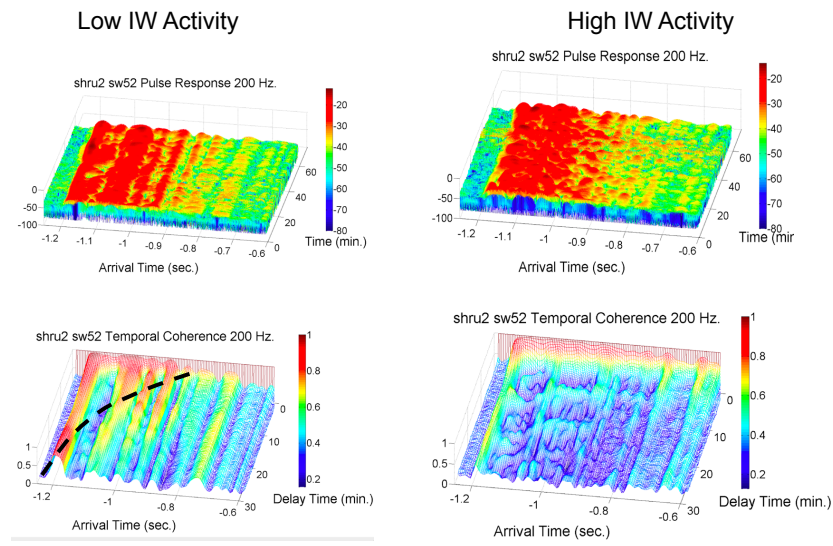
Figure 1.4: 100Hz SW06 data during high IW activity (top left) and coherence (bottom left) and during low internal wave activity mode structure (top right) and coherence (bottom right)

cases, the discussions of the pervious section become relevant. Since the acoustic signals traverse over the same bottom (static source and receiver configuration), it is only the ratio of acoustic wavelength to bottom fluctuations that changes as frequency increases. The data follows the same result of the modeled propagation where, as that ratio increases, the mode stability decreases contributing to the loss of coherence.

Figure 1.7 illustrates the pulse response data and temporal coherence calculation results from the Florida Straits experiment. The same trends are present. Lower order modes have a longer coherence time than higher order modes and coherence is lost quicker at higher frequencies. However there is one difference: coherence times are on average longer here than for the SW06 experiment. The water column depth may be of influence here.

Finally, the spatial coherence results for the Acoustic Observatory experiment are
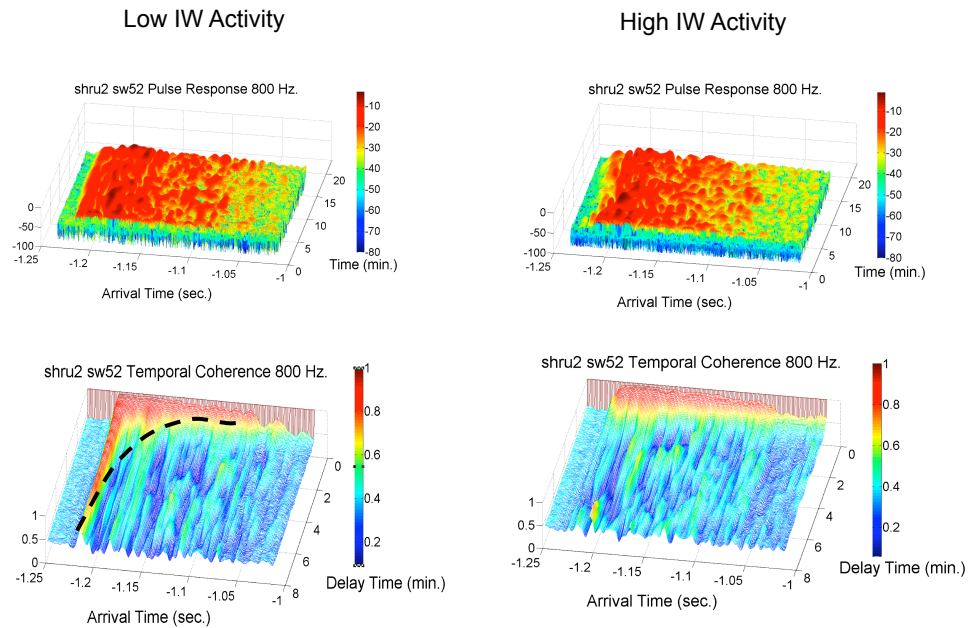
Figure 1.5: 200Hz SW06 data during low IW activity (top left) and coherence (bottom left) and during high internal wave activity mode structure (top right) and coherence (bottom right)

presented in Figure 1.8. Here spatial coherence is on the order of 15 wavelengths with the first mode exhibiting the longest coherence time. Summarizing, there are consistent and universally observed experimental results that cannot be explained by IW activity alone. It is found that:

- Low frequencies (<100 Hz). Bottom appears smooth, mirror-like reflections of all mode angles. Clean separable modes. Coherence depends only on sound speed variability. All modes have equally long coherence times.

- Mid frequencies (200→800 Hz). Affected by both bathymetry and sound speed. Low order, low grazing angle modes are always more coherent than higher order, higher grazing angle modes. Steeper mode angles see more of bottom variability. Late modes are more smeared.

Low IW Activity
High IW Activity

shru2 sw52 Pulse Response 800 Hz.

shru2 sw52 Pulse Response 800 Hz.

shru2 sw52 Temporal Coherence 800 Hz.

shru2 sw52 Temporal Coherence 800 Hz.

Figure 1.6: 800Hz SW06 data during low IW activity (top left) and coherence (bottom left) and during high internal wave activity mode structure (top right) and coherence (bottom right)

- High frequencies (>800Hz.) Only first mode has usable coherence even with no measurable internal waves. Higher order modes are smeared when bathymetry. Modes merge and become continuous losing all coherence.

- Spatial coherence similar - higher order modes→lower coherence length, further suggesting this is a bottom effect and not caused by internal waves.

- Limits on coherence at higher frequencies depend on bottom bathymetry and not on internal waves. When modes are randomized by bottom irregularities even slight changes in sound speed and/or source/receiver motion will de-correlate signals in space and time.

These three experiments and the results presented here provide the backbone
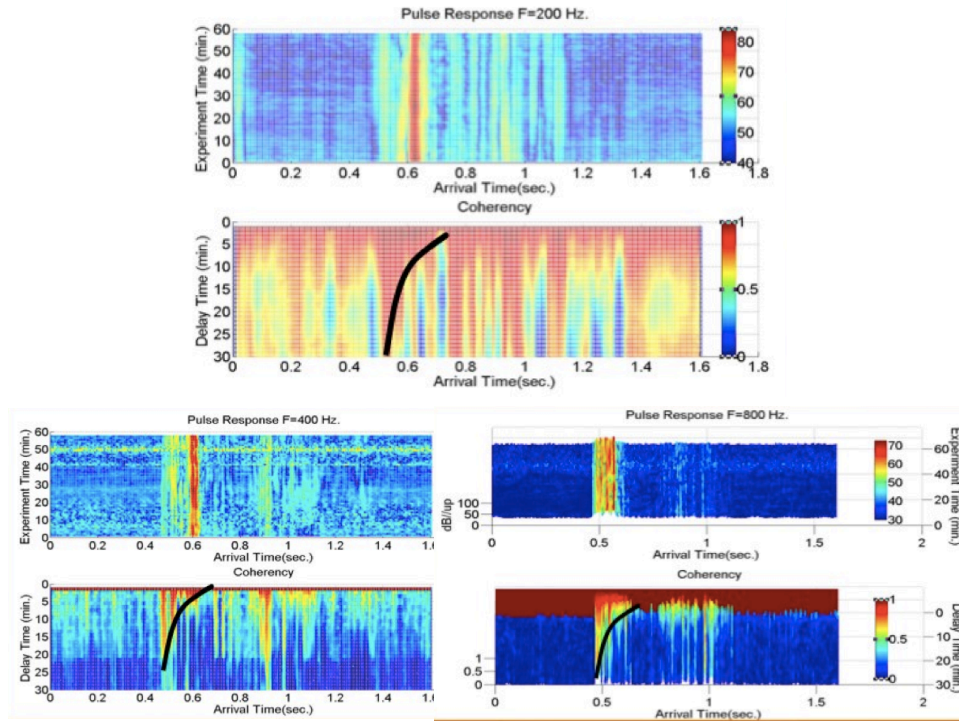
Figure 1.7: Pulse response and temporal coherence data from the Florida Straits experiment at (top) 200Hz, (bottom left) 400Hz, and (bottom right) 800Hz.

and motivation behind this work. The chapters presented herein will be divided as follows. Chapter 2 will discuss the methodology behind the work presented, discussing both modeling of sound field fluctuations and bottom bathymetry. In addition, the types of coherence will be examined. Chapter 3 will focus on the effects of bottom bathymetry on mode structure. Here we wish to examine how the mode structure becomes randomized and what degree of bathymetric fluctuations are needed to cause a loss of structure. A mode coherence calculation will be computed in order to quantify this randomizing effect. In addition the effects of both depth and range variations on mode coherence will be examined. Chapter 4 will examine the effects of ship motion on temporal coherence. Three different tracks will be used: a parallel moving source and receiver, a tangential ship track around a stationary source, and
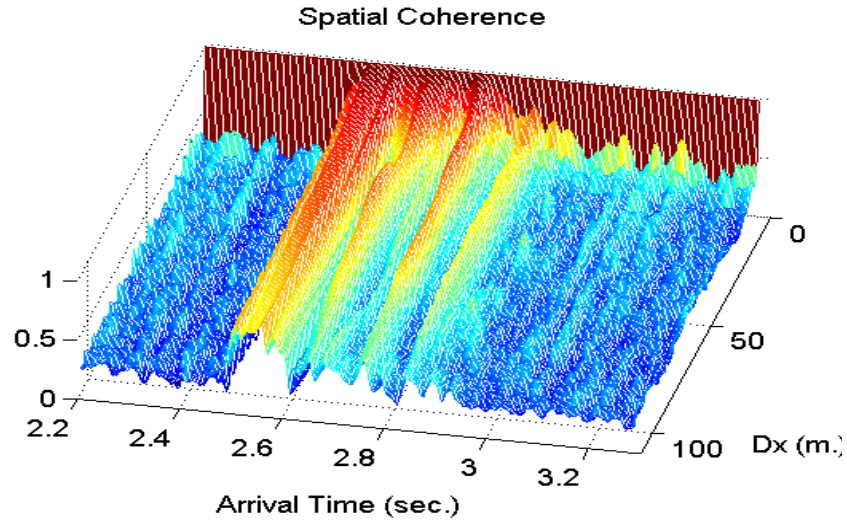
Spatial Coherence

Figure 1.8: Spatial coherence results from the Acoustic Observatory experiment

a radial ship track moving outwards from a stationary source. In Chapter 5, sound field fluctuations will be added into the modeling work in order to calculate temporal coherence. Several different levels of sound field fluctuations will be discussed with the goal of understanding the joint effect of both bottom bathymetry and internal waves on the loss of coherence. Finally Chapter 6 will summarize all of the finding in the conclusions

Chapter 2
Methodology

It is shown in Chapter 1 that data from the experiments show distinct arrivals from surface-reflected/bottom-reflected (SRBR) modal arrivals. Each of these arrivals has a corresponding group velocity. Normal modes are low loss and coherent elemental(single) transmission paths in shallow water. The goal of this dissertation is to understand how these transmission paths are randomized and how they, in turn, randomize signals transmitted through them. Instead of examining the effect of coupling between modes, a simple PE modal arrival coherence calculation will be introduced. By examining just the received signal the calculations discussed are similar to those evaluated on the experimental data. Figure 2.1 demonstrates the agreement between the SW06 data and the MMPE model with clean separable arrivals visible in both.
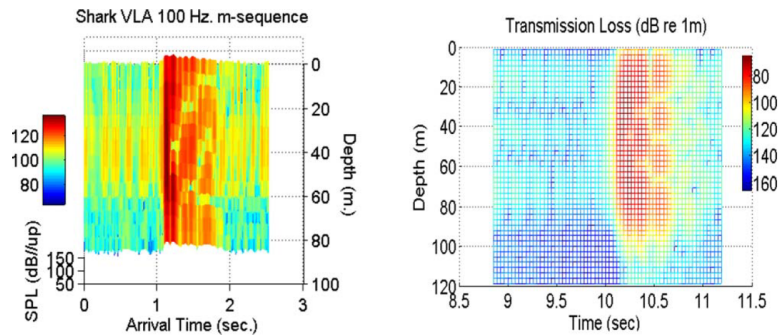
Figure 2.1: Comparison between SHARK vertical array data (SW06 experiment) and MMPE arrivals

The remainder of this chapter will be devoted to discussing the environmental

data used in the model and the reasons for and descriptions of the calculations using model generated estimates.

2.1 Bathymetric Modeling

In order to examine the effect of bottom bathymetry on modal arrival coherence a "pseudo" random bottom model is created with the goal of introducing bottom fluctuations that appear locally smooth over the footprint of the acoustic reflection. A simple model is used in which high frequency fluctuations are filtered from a set of Gaussian distributed random numbers, ensuring localized bottom scattering would be eliminated. The methodology for creating this bottom is illustrated in Figure 2.2 and a typical correlation length of this bottom is illustrated in Figure 2.3.

The general formulation to creating this bottom is as follows. First a random variable is called with numbers at range points, x, and RMS amplitude of 1.

$$S(x) = rand(x). \tag{2.1}$$

The bottom is Fourier transformed such that

$$S(k) = \mathcal{F}[S(x)](k). \tag{2.2}$$

A lowpass filter is then applied to allow any wavelengths (lowpass since it is filtered in wavenumber) above the minimum wavelength to pass. The remaining data is then filtered with a 25% cosine bell function which takes the form

$$
w(n) = \begin{cases} \frac{1}{2}[1 - cos(\frac{\pi i}{n})], & \text{if } 0 \leq n \leq \frac{N}{4} \\[2mm] 1, & \text{if } \frac{N}{4} < n < \frac{3N}{4} \\[2mm] \frac{1}{2}[1 - cos(\frac{\pi i}{n})], & \text{if } \frac{3N}{4} \leq n \leq N \end{cases}
$$

Here N is the number of nonzero points after applying the lowpass filter. The data is

filtered using $w(n)$

$$
S(k) = S(k) * w(n); \tag{2.3}
$$

and inverse Fourier transformed

$$
S(x) = \mathcal{F}^{-1}[S(k)](x). \tag{2.4}
$$
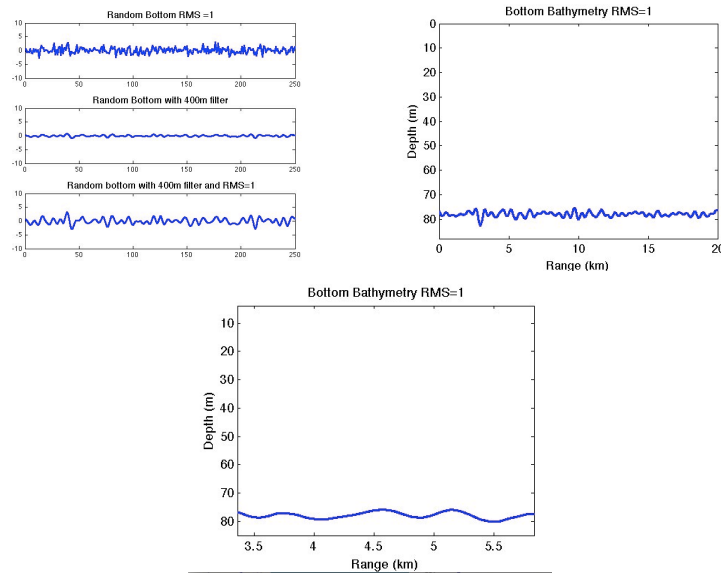
Figure 2.2: Bottom Bathymetry Example

In addition to using the bottom bathymetry in 2D model runs, it is expanded

to a random 3D bottom to allow for Nx2D model runs (Nx2D neglects coupling
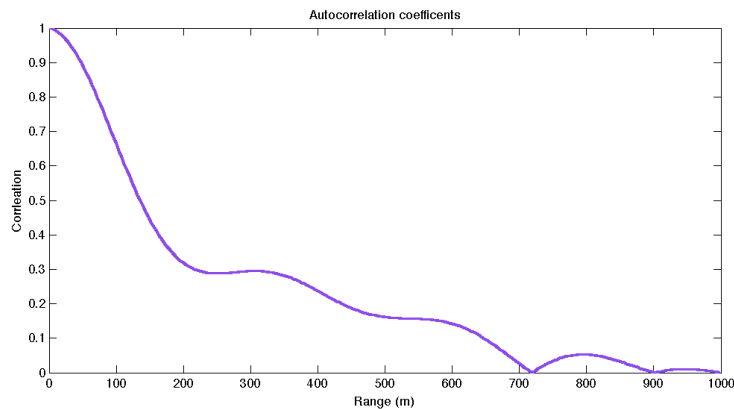
Figure 2.3: Autocorrelation Function of a Sample Random Bottom

between radials resulting in a faster run time than a full 3D model.) The method for creating the 3D bottom is exactly the same as the 1D bottom model but filtering is performed both in the range and cross range direction. This version is used for modeling ship motion and spatial coherence calculations. The methodology as the original 2D format is the same; however, now filtering is done in both range and cross range. An example of this is shown in Figure 2.4.

2.2 PE Modal Arrival Coherence Calculation

The bathymetric variations (section 2.1) are introduced into the MMPE model with the water column sound field held constant in order to investigate the effect of bottom bathymetry on modal arrival structure.The RMS amplitude is increased by fractions of the acoustic wavelength and the acoustic field recalculated for each case.

Figures 2.5 to 2.8 illustrate the arrival shapes and phase variations for each individual mode and various RMS bottom levels. The first arrival, dominated by mode
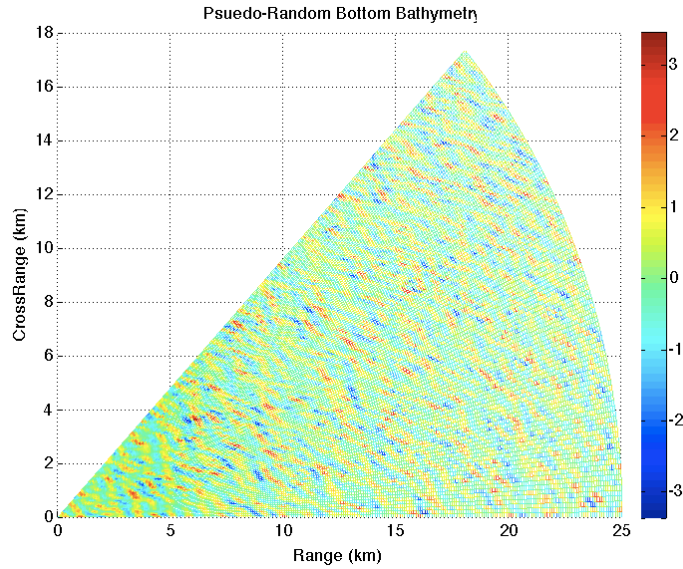
Figure 2.4: An example of the 3D bottom modeling used to approximate ship motion
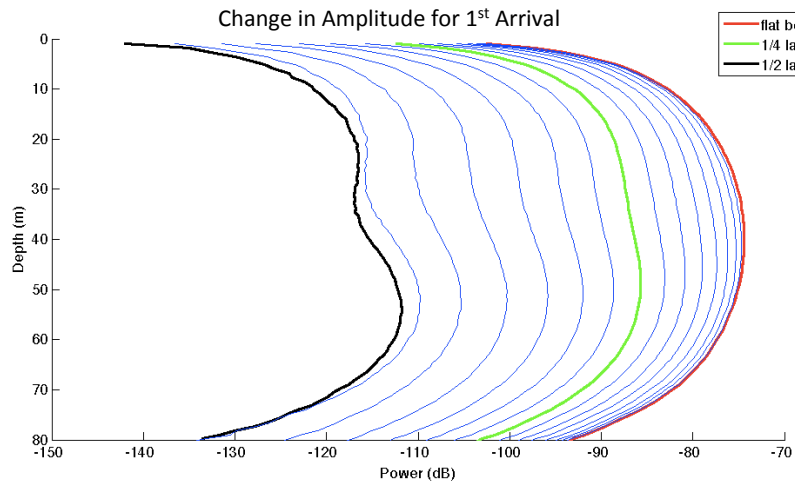
Figure 2.5: Amplitude for the first arrival at 100Hz and various bathymetric variations

1, which has limited bottom interaction, maintains a fairly stable shape. However as bottom RMS increases power is lost. The arrival shape becomes slightly more unstable for the second arrival dominated by mode 2, and the phase shift becomes slightly more erratic with increasing bathymetry variations. However, in the 3rd and
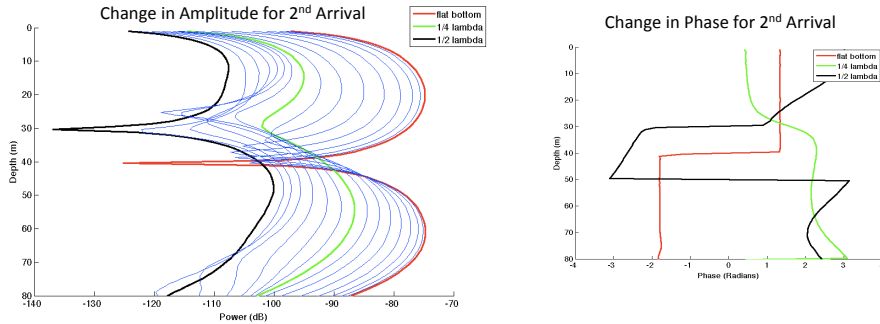
Figure 2.6: Amplitude and Phase for Mode 2 at 100Hz and various bathymetric variations

4th arrivals the effects of bottom bathymetry are most clearly visible. With increasing RMS, modal amplitude decreases and mode shape and phase become irregular. Noise becomes a dominating factor, especially for the fourth arrival.

The PE modal arrival coherence (PEMAC) calculation is introduced here in order to clearly and simply represent the change in phase and amplitude of a mode due to environmental influences, such as bathymetry variations. The ideal case (flat bathymetry, flat surface, and constant sound speed profile) will be used as the benchmark case to which all other cases will be compared. In much the same way that a temporal coherence calculation folds the amplitude and phase into a single equation, the modal arrival coherence calculation does the same.

PEMAC is defined as the depth average correlation function between the ideal modal arrival structure for the water column and the mode structure resultant from a RMS bottom realization. The PEMAC is a statistical representation of the coherence at any given point in the water column and isn't dependent on hydrophone location
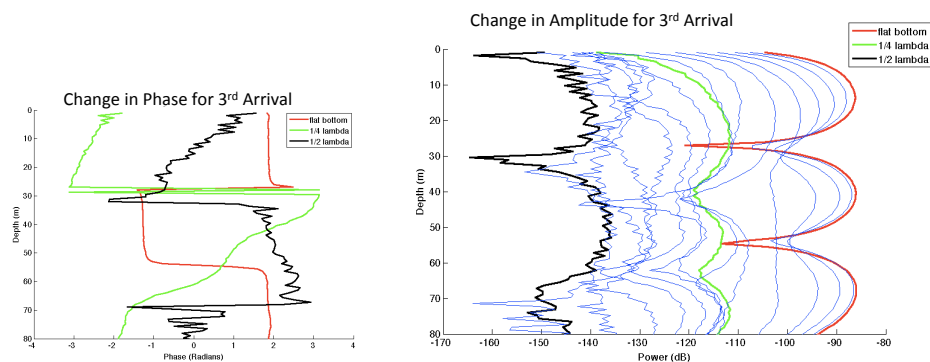
Figure 2.7: Amplitude and Phase for Mode 3 at 100Hz and various bathymetric variations
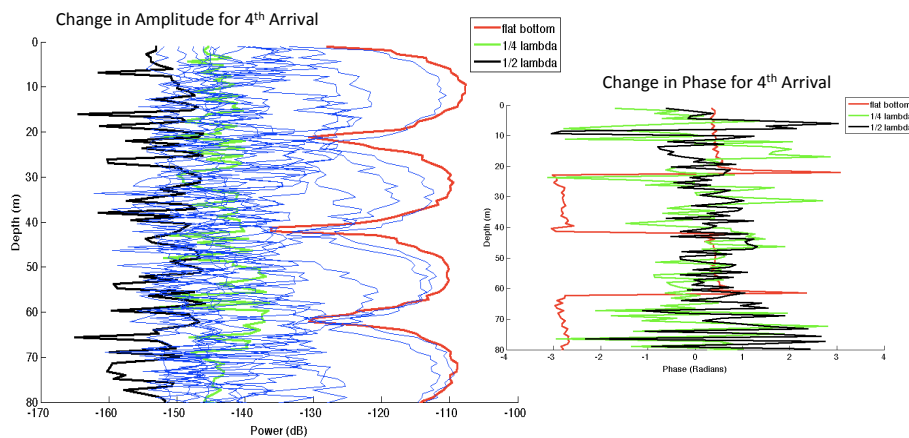
Figure 2.8: Amplitude and Phase for Mode 4 at 100Hz and various bathymetric variations

such as temporal coherence. The equation for PEMAC used here is as follows:

$$mcoh(t) = \frac{< p_o(z,t) p_n(z,t)) >_{\Delta z}^2}{< p_o(z,t)^2 >_{\Delta z} < p_n(z,t)^2 >_{\Delta z}}. \tag{2.5}$$

Here p_o is the pulse response structure from the flat bottom ideal case and p_n is the pulse response structure to a case with fluctuations added which is summed over

depth, z. PEMAC is dependent on modal arrival structure. The less sensitive the acoustic modes are to changes, i.e. the greater the arrival structure coherence, the greater temporal coherence will be. Clean, well defined modal arrivals result in high mode coherence, while modes lacking a clear structure have low PEMAC.

PEMAC is a measure of acoustic mode sensitivity to changes in environment or path. These changes can include bottom bathymetry variation, source-receiver motion, and sound speed variability in the propagation channel. Therefore, PEMAC is a function of mode number (MN), range (R), RMS bottom variability, acoustic frequency (F), depth(D), and the source velocity (S) in the most general case.

2.3 Temporal Coherence

Temporal coherence of individual arrivals will be computed from results presented in this paper. Temporal coherence has been the most standardly used definition of coherence in previous literature and is defined as the statistical measure of the similarity of a waveform in time. It is a complex quantity that depends on both the amplitude and phase of a waveform.

The temporal coherence is computed as a time lagged covariance function of the following form:

$$coh(t,\tau) = \frac{< p(t,T)p(t,T+\tau)) >^2_{\Delta T}}{< p(t,T)^2 >_{\Delta T} < p(t+,T+\tau)^2 >_{\Delta T}}. \tag{2.6}$$

Here p(t) is the channel pulse response, t is the arrival time, T is the experimental time and τ is the coherence lag time. Normally the coherence would be calculated

over a time averaged section of $p(t)$ resulting in one value encompassing all of the mode arrivals, including the effects of multi path interference. However here, the time lagged cross product will be computed over the time history sections of p(t). The resultant is a coherence value for every arrival time, t, at each coherency lag, τ, which allows for the individual arrival coherencies to be analyzed.

Usually the calculation is computed for a single hydrophone in the water column over time. However this calculation can present an incomplete representation of coherence as the location of the hydrophones becomes important. If the hydrophone is located at a node for a given mode, the coherence for that mode will be reduced, but if the hydrophone is moved several meters in the water column the coherence may once again become significant.

There are two ways coherence can be lost, deterministic and random. A deterministic loss of coherence is one that, in theory, can be recovered. An example of such is a slow phase shift in the acoustic signal induced by a slowly varying sound speed. A random loss is one that is unrecoverable.

While the PEMAC calculation acts as a comparison between the actual and ideal pulse response, the temporal coherence calculation can be expanded upon as well for temporal coherence. At any one experimental time the pulse response can be written as

$$P(d,t) = A(d,t)e^{i\theta(d,t)}. \tag{2.7}$$

Here A is the amplitude of the arrival and θ is the phase. If small random perturbations are introduced to the bottom (or the sound speed profile), the pulse response

will be changed by a small amount,

$$P(d,t) = P_i(d,t) + \delta P(d,t). \tag{2.8}$$

Here $P_i(d,t)$ is the pulse response to an ideal channel and $\delta P(d,t)$ is the perturbation caused by interaction with the environment. The temporal coherence calculation can now be expanded out in terns of $P_i(d,t)$ and $\delta P(d,t)$ as

$$coh(t,\tau) = \frac{< (P_i(t,T) + \delta P(t,T))(P_i(t,T+\tau) + \delta P(t,T+\tau)) >^2_{\Delta T}}{< (P_i(t,T) + \delta P(t,T))^2 >_{\Delta T} < (P_i(t,T+\tau) + \delta P(t,T+\tau))^2 >_{\Delta T}}. \tag{2.9}$$

However $P_i(t,T) = P_i(t,T+\tau)$ because the amplitude and phase of the ideal pulse response remain constant in time. The temporal coherence calculation then be expanded out and becomes

$$coh(t,\tau) = \frac{< (P_i(t,T)^2 + P_i(t,T)[\delta P(t,T+\tau) + \delta P(t,T)] + \delta P(t,T)\delta P(t,T+\tau) >^2_{\Delta T}}{< (P_i(t,T) + \delta P(t,T))^2 >_{\Delta T} < (P_i(t,T) + \delta P(t,T+\tau))^2 >_{\Delta T}}. \tag{2.10}$$

The coherence is now clearly dependent upon the summation of the ideal pulse response, the perturbation introduced by the environment and the cross terms between the two.

2.4 Sound Field Modeling

Several different approaches are taken for modeling the sound speed variability. The first of which is to introduce a simple sinusoidal sound field fluctuation onto a mean

continuous sound speed profile. The fluctuation varied slowly in range with a period on the scale of 3km and is contained mainly in the mid depths and tapering off such that the sound speed remained constant in the upper 10m and lower 20m of the water column. The resultant merely shifts the sound speed points in depth while maintaining the continuous nature of the whole sound speed profile. The goal of the temporal fluctuation is not to introduce scattering into the water column but rather to introduce a fluctuation that produces a deterministic loss of temporal coherence when there is no bottom effect. This loss, in theory, would be recoverable producing only a shift in phase due to the slow time variation and adiabatic shifting of the modes across the receiver. When combined with the bottom bathymetry model, this allowed for an investigation into the effect of bottom bathymetry on temporal coherence while reducing any random coherence loss due to water column fluctuations. For each different bottom realization, the temporal coherence is computed for 30 minutes with 30s sampling. This modeling is used for the calculation of temporal coherence.

The second approach to modeling the sound field is to model the small scale IW fluctuations. The goal of the small scale sound field modeling is not to model non-linear internal waves directly, but rather to create a simple model with easily definable parameters that could be quickly varied computationally for use in the MMPE. The same type of sinusoidal fluctuation as above is used, however the length scales are altered. For the purposes of this paper, the wavelength of the fluctuations is set at $350m$ and the wave height is varied between $0m$ and $20m$ in $1m$ increments. These values come from an examination of the SW06 sound field data and previous literature on the modeling of sound field variations. It has been found in previous
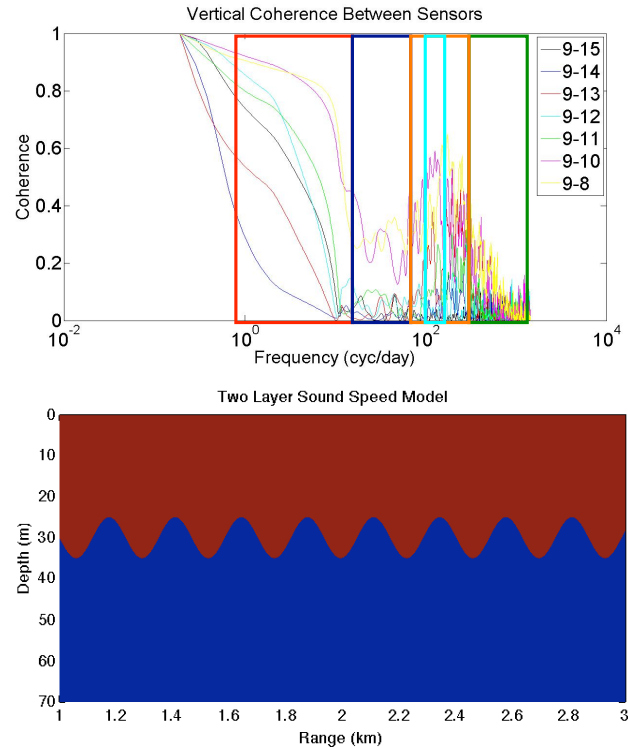
Figure 2.9: (Top) The vertical coherence between the sensors of the SHARK array. (Bottom) Image of amplitude and length scales used for modeling of high frequency internal waves

literature that internal wave wavelengths can vary between 200m and 600m with wave heights of up to 20m[33]. The bottom panel of Figure 2.9 presents a example of the sound field model used and the top panel is the vertical coherence between sensors of the SHARK array. Located in the light blue box of this figure is the increase in coherence caused by high frequency internal waves. Using an average internal wave speed between $0.5 m/s$ and $1 m/s$ and a center frequency of 160 cycles per day for the internal wave energy, the wavelength of the internal wave field is calculated to vary between approximately $250 m$ and $550 m$. This places the $350 m$ used here well within the estimates. The bottom panel of Figure 2.9 illustrates the scales of the fluctuation used however here the mean background profile has been removed for clarity of scales.
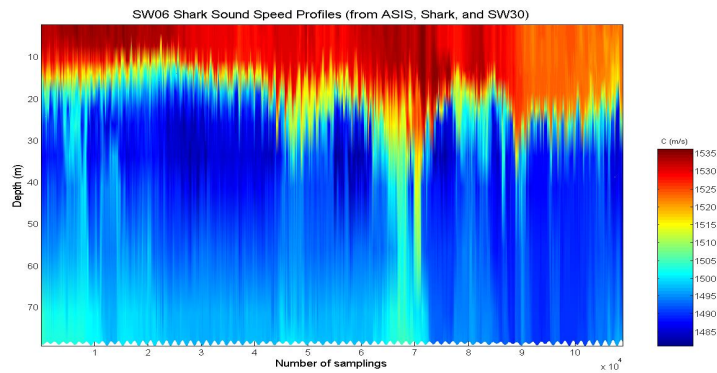
Figure 2.10: Temperature data from the SHARK array

The purpose of this modeling is to understand the effects that small scale sound field variations can have on mode coherence.

Data is used from a 2hr period of high internal wave activity as measured by thermistors from the SHARK array (Figure 2.10) for the third approach to IW modeling. When importing the data to the MMPE model only one sound speed profile is used for the entire 20km range, with a new profile being used for every 30s of data, which is the resolution of the thermistor data. This approximated an internal wave train traveling perpendicular to the acoustic travel path in question. The data appeared to be sufficient to resolve all the major variations in the sound speed column.

The original SHARK data is banded into frequency bands to reduce noise, and only a narrow band centered on the IW frequency of 160 cycles per day is used to include internal wave fluctuations in the calculation. This band is illustrated in the top image of Figure 2.9 and presents the vertical coherence between the SHARK array sensors with the IW band being centered around the uptick in coherence boxed around here in light blue. This is then combined with the bottom bathymetry modeling and used to model temporal coherence when both internal waves and bottom variations are present.

Chapter 3
PE Modal Arrival Coherence

In this chapter the effects of bathymetric variations on PE mode coherence will be examined. The bathymetric fluctuations described in section 2.1 are used with a constant sound speed profile. The RMS amplitude is increased by fractions of the acoustic wavelength and the acoustic field recalculated for each case. Finally, the depth-averaged PEMAC is computed in each instance.
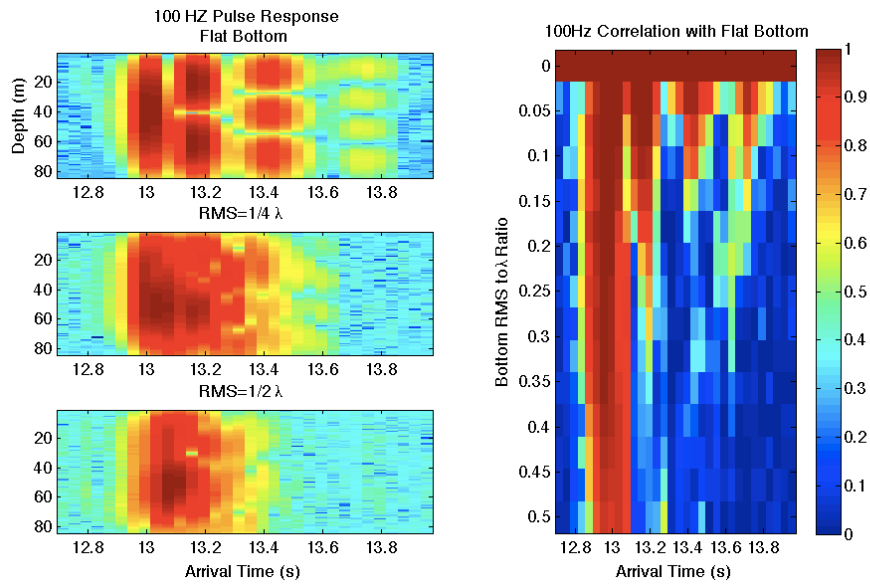
Figure 3.1: (Left) PE model prediction of pulse response at 100Hz for a flat bottom, $\frac{1}{4}\lambda$ RMS bottom and $\frac{1}{2}\lambda$ RMS bottom, (Right) PEMAC predictions for 100Hz.

Figure 3.1 presents the results for the low frequency limiting case of 100Hz with the model calculation being done at a range of 20km. While Figures 3.2 and 3.3 present the results for the mid-range frequencies at 200Hz and 800Hz ,respectively, both at a range of 20km. These frequencies and ranges are chosen to compare with the experimental geometry of the SW06 experiment.
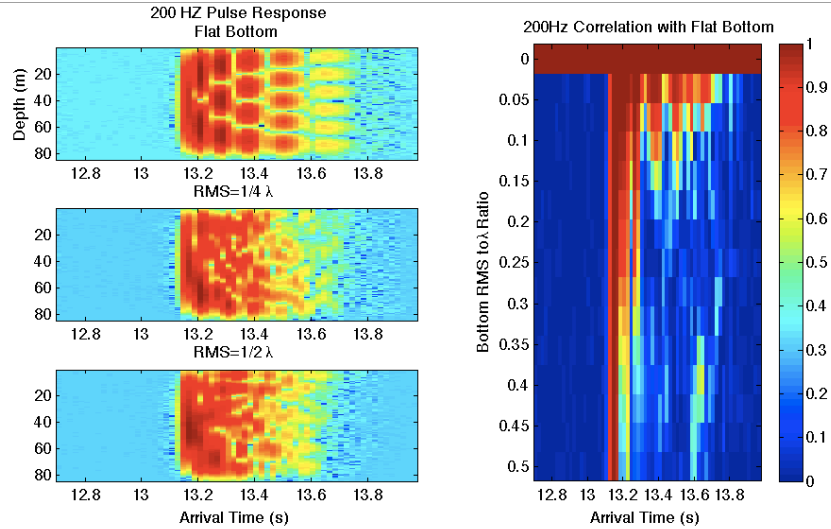
Figure 3.2: (Left) PE model prediction of pulse response at 200Hz for a flat bottom, $\frac{1}{4}\lambda$ RMS bottom and $\frac{1}{2}\lambda$ RMS bottom, (Right) PEMAC predictions for 200Hz.
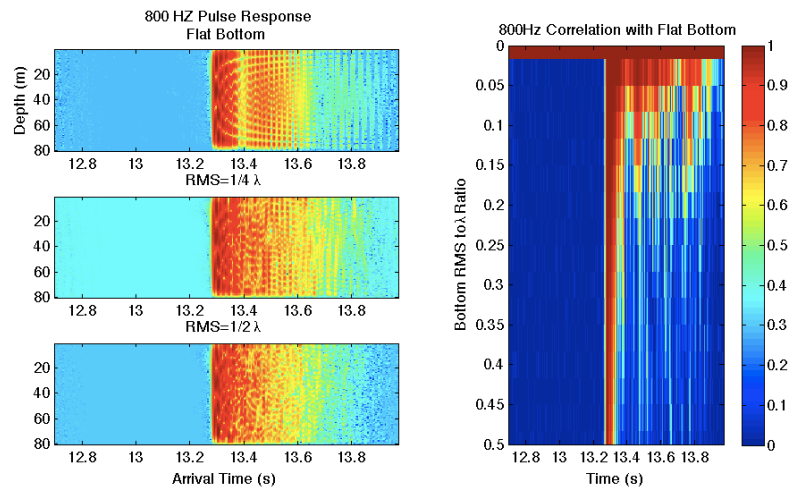
Figure 3.3: (Left) PE model prediction of pulse response at 800Hz for a flat bottom, $\frac{1}{4}\lambda$ RMS bottom and $\frac{1}{2}\lambda$ RMS bottom, (Right) PEMAC predictions for 800Hz.

In Figure 3.1 the left panel presents the arrival time data for the 100Hz modeling results. The upper plot is the flat bottom case and here the number of modes is only limited by strong bottom loss that occurs with increased grazing angles at higher mode numbers. The middle plot is pulse arrivals where there is a bathymetric variation of RMS amplitude $\frac{1}{4}\lambda$ or approximately 3.75m. Here, while the first couple of modes

remain intact, there has been a loss of structure for the latter arrivals. Finally the bottom pane presents the results with a bathymetric variation of $\frac{1}{2}\lambda$ or 7.5m. Here, only the first mode remains intact and the remaining energy has been distributed amongst the latter arrivals with boundaries between modes becoming smeared. The PEMAC results with RMS bottom amplitude increasing from zero to $\frac{1}{2}\lambda$ in small increments is shown in the right panels of Figures 3.1 - 3.3. The first mode remains coherent across all of the bathymetric variations. However, all other arrivals lose coherence with the higher order modes more sensitive to the bathymetric variations than the lower order ones.

Figures 3.2 and 3.3 exhibit consistent results with the 100Hz case; however with a larger number of arrivals being included in the PEMAC calculation due to grazing angle considerations. Here the maximum RMS amplitudes included in the calculations for the 200Hz and 800Hz cases are approximately 3.75m and 1m, respectively.

Depth Effects

In addition to the depths and frequencies covered by the SW06 experiment, the depth of the bottom is increased and the model rerun at each frequency in order to compare data from the AOCE and FL Straits experiment.

Figure 3.4 presents the PEMAC data at 100Hz with water column depths of 100m and 200m. These depths are chosen as intermediary depths as the depth of the Fl Straits experiment is approximately 140m and the the depths of the Acoustic Observatory experiment is approximately 250m. Once again the range is chosen as 20km.
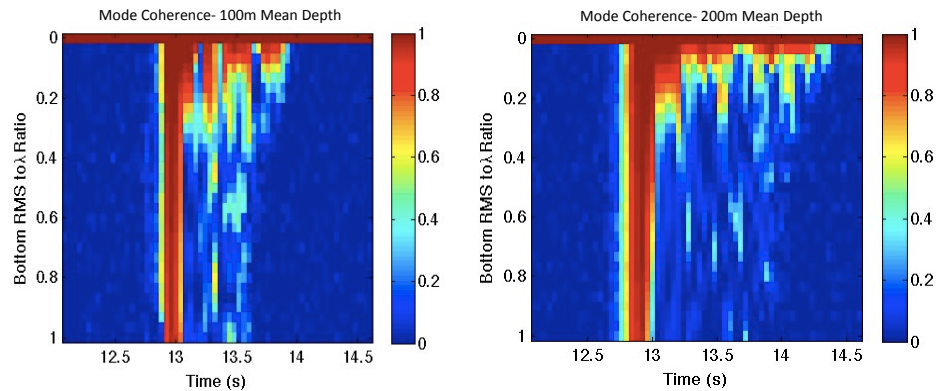
Figure 3.4: (Left) PEMAC predictions at 100Hz frequency and 100m water column depth, (Right) PEMAC predictions at 100Hz frequency and 200m water column depth.
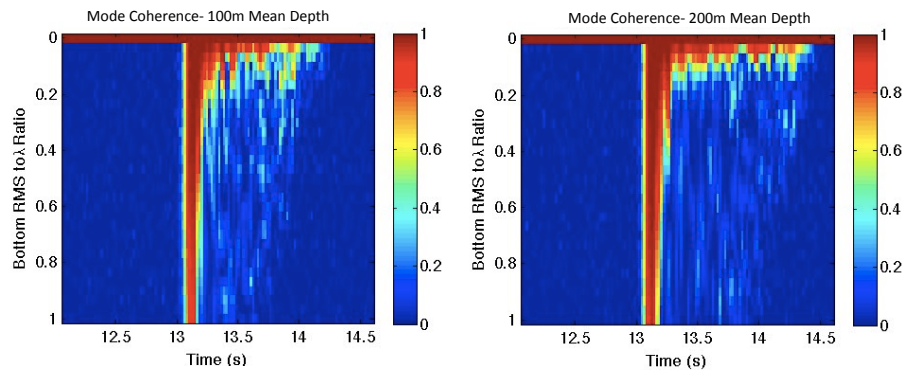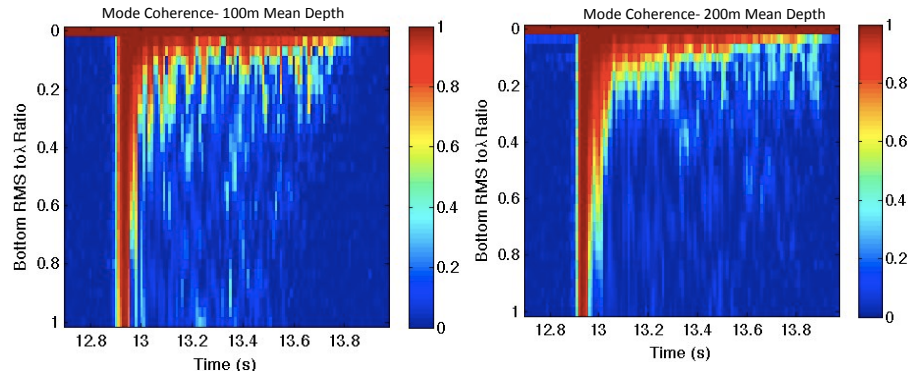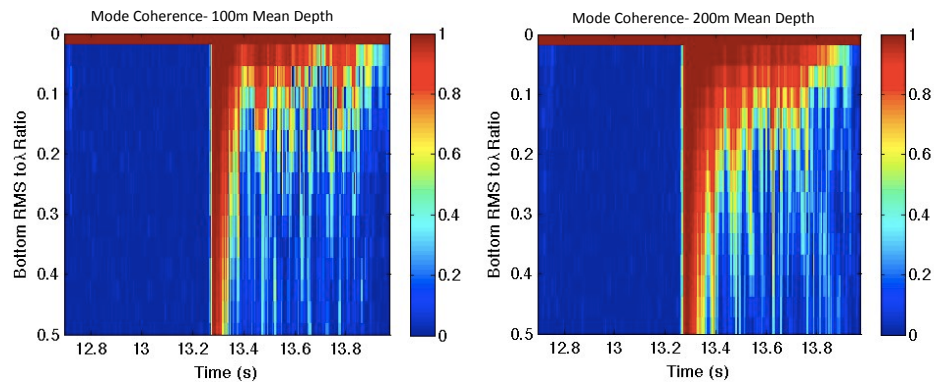

Figure 3.5: (Left) PEMAC predictions at 200Hz frequency and 100m water column depth, (Right) PEMAC predictions at 200Hz frequency and 200m water column depth.

Figures 3.5-3.7 are the similar data as in Figure 3.4 but at 200Hz, 400Hz, and 800Hz, respectively. Similarities exist here once again between the model data and experimental data. At the lower end of frequencies, the results remain similar between the two depths in question except results have become spread out in time. However, as frequency is increased, PEMAC increases with depth with the same RMS bottom

Figure 3.6: (Left) PEMAC predictions at 400Hz frequency and 100m water column depth, (Right) PEMAC predictions at 400Hz frequency and 200m water column depth.

Figure 3.7: (Left) PEMAC predictions at 800Hz frequency and 100m water column depth, (Right) PEMAC predictions at 800Hz frequency and 200m water column depth.

fluctuations. These results are consistent with the findings of the Florida Straits experiment. As before, the higher frequencies exhibit more coherence than those of similar frequency from the SW06 experiment. While a possible explanation from the experiment results could be a difference in bottom bathymetry, another explanation is the increase in depth. As depth increases, bottom fluctuations become a smaller

overall fraction of the acoustic travel path and therefore carry less importance in the loss of coherence.

Range Effects

While there is no experimental data directly influencing this next section, it is decided to examine the effect of range on PEMAC . Once again the bottom is varied in RMS going from flat to 0.5λ in 0.1λ increments. The same PEMAC calculation as above is computed, however the final output is displayed as a function of range. Figure 3.8 presents the results at 100Hz at depths of 100m and 200m. Mode arrivals spread out in time as the range increases which accounts for the spreading out in time of the images produced here. Clear trends can be seen, however. As range increases, the later order arrivals are not as coherent as they are at shorter ranges while the first mode remains coherent at all ranges. As RMS bottom , the coherence is lost quicker. This indicates that at shorter ranges mode structure remains more stable than at longer ranges for variable bathymetry. This is due to the number of interactions with the bottom that the acoustic signal makes as there is a great chance for a higher number of bottom interactions as the range increases.
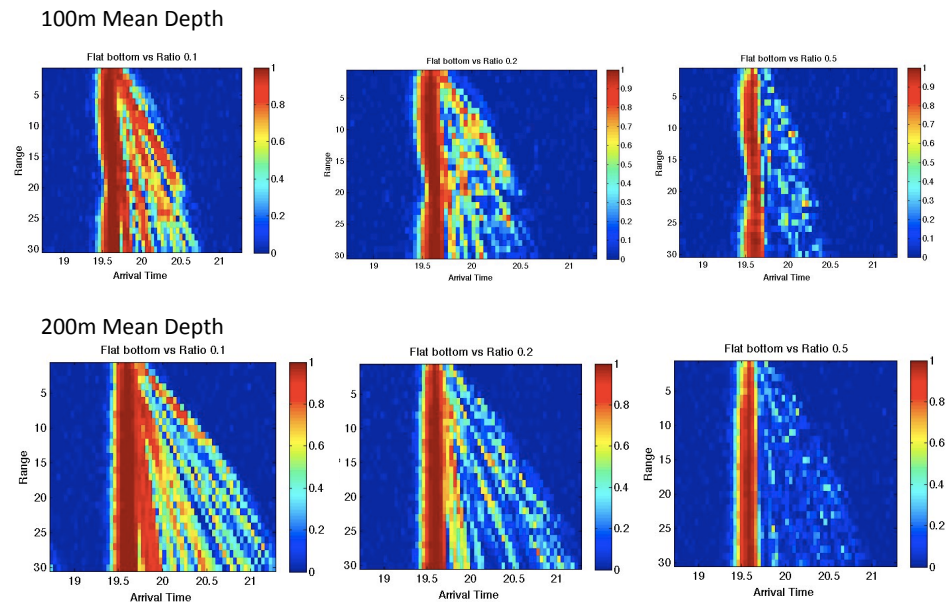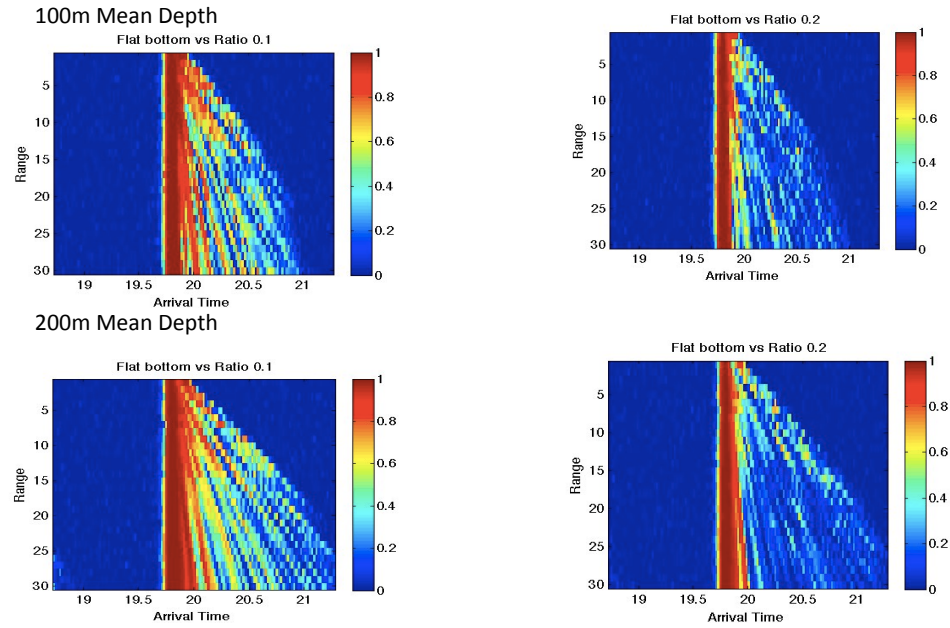
Figure 3.8: (Top) PEMAC predictions at 100Hz frequency and 100m water column depth. Range variation is the y-axis and the far left is a RMS bottom ratio of 0.1 the middle is a RMS bottom ratio of 0.2 and the far right is a RMS bottom ratio of 0.5 , (Bottom) PEMAC predictions at 100Hz frequency and 200m water column depth.

Figures 3.9 and 3.10 illustrate the range dependent PEMAC results at 200Hz and 800Hz. The results are consistent with those of 100Hz for similar RMS bottom amplitude to acoustic wavelength ratios. These plots are also another indication of the effect of depth on PEMAC as discussed in the previous section. Higher PEMAC is present as mean depth increases.

Figure 3.9: (Top) PEMAC predictions at 200Hz frequency and 100m water column depth. Range variation is the y-axis and the far left is a RMS bottom ratio of 0.1 and the far right is a RMS bottom ratio of 0.2 , (Bottom) PEMAC predictions at 200Hz frequency and 200m water column depth.
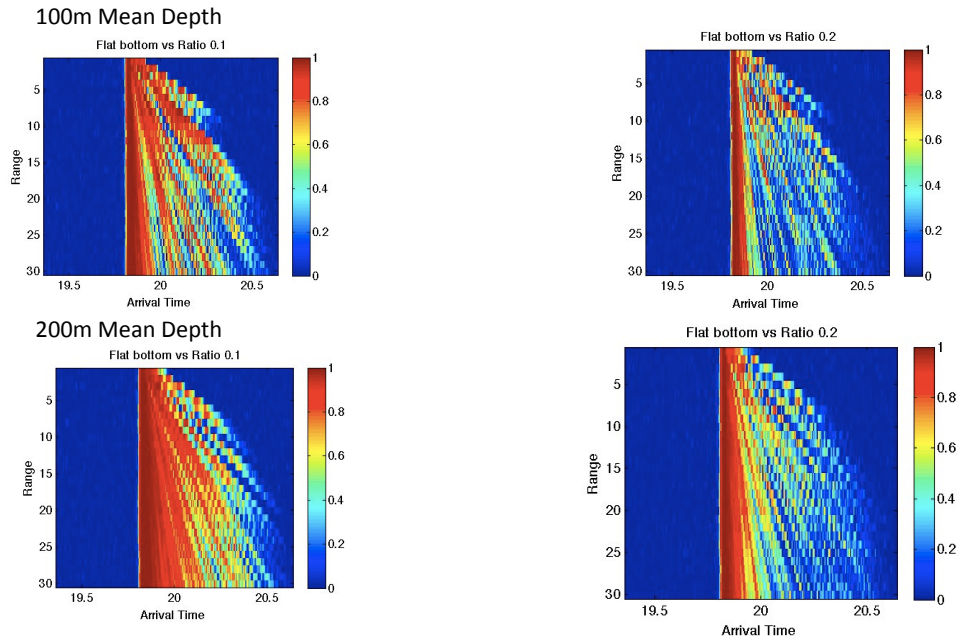
Figure 3.10: (Top) PEMAC predictions at 800Hz frequency and 100m water column depth. Range variation is the y-axis and the far left is a RMS bottom ratio of 0.1 and the far right is a RMS bottom ratio of 0.2 , (Bottom) PEMAC predictions at 800Hz frequency and 200m water column depth.

Chapter 4
Moving Platforms

The effects of ship motion on temporal coherence are discussed in this chapter. Three different source receiver geometries are used. A source and receiver towed in parallel 20km apart at a ship speed of 2kts is the first. The second geometry is a stationary source with a receiver moving tangentially around the source. A stationary source with a receiver propagating outward from the source is the third. Calculations are run at intervals of 30s. The effects of water column variability are ignored and a simple sound speed profile, which remains constant over the propagation path, is used

The MMPE model is run with multiple times for each different path with the bot-
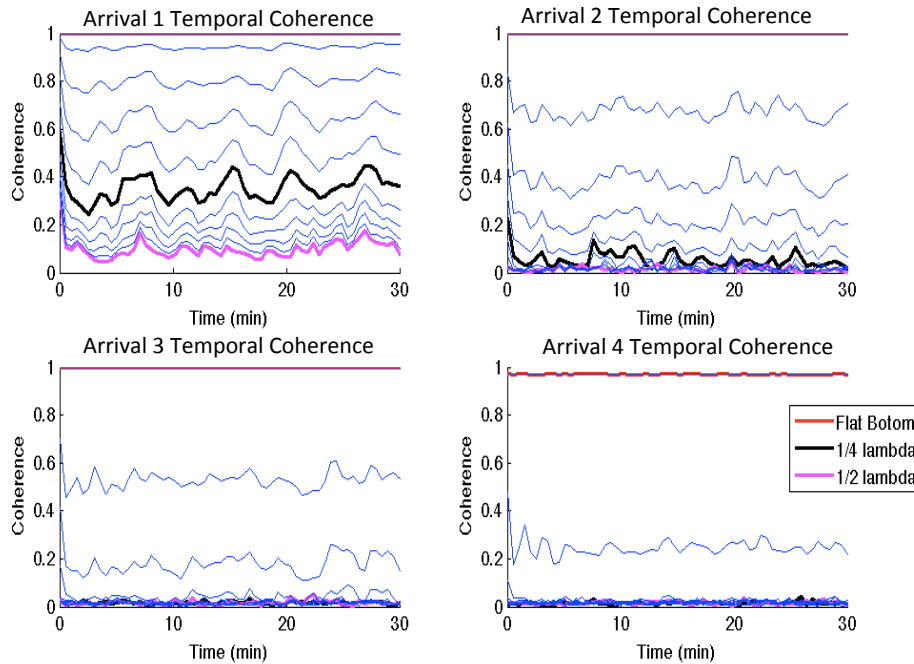
Figure 4.1: Temporal coherence for the first four arrivals from a 100Hz signal at a range of 20km and a parallel tow path with a ship speed of 2kts.

50

tom bathymetry varying as a function of RMS bottom amplitude. Previous sections have indicated that it is the ratio of RMS bottom amplitude to acoustic wavelength (λ) that is important to coherence calculations and so bathymetric fluctuations are restrained between a flat bottom and $\frac{1}{2}\lambda$ in 0.05λ increments.

Figure 4.1 illustrates the temporal coherence results for arrivals 1-4 at varying RMS bottom amplitudes and the parallel tow case. As expected, with a flat bottom the arrivals remain fully coherent over the entire calculation time. As RMS bottom amplitude increases coherence decreases. Additionally, arrivals 3 and 4 have shorter coherence times than modes 1 and 2 for the same bathymetric fluctuations. However, the coherence remains at a steady level over much of the calculation time. This is expected as there are no temporal fluctuations included in the calculation and only the bottom bathymetry is causing a loss of temporal coherence.

Figure 4.2 illustrates the mean PEMAC for the parallel tow case. PEMAC is lost as RMS bottom amplitude increases and the loss is greater for the higher order modes. This is as expected and is consistent with the results presented in Chapter 3. Figures 4.3 and 4.4 graph the PEMAC vs temporal coherence for arrivals 1-4. As PEMAC decreases, so does temporal coherence. There is a cutoff point for the PEMAC, around 0.4, after which temporal coherence is completely lost. While the parallel tow case is a simple example, the results are clear and important. PEMAC and temporal coherence are linked. Even when no sound speed fluctuation is present with a slow moving source-receiver geometry small variations in bottom bathymetry can be the main cause for the loss of temporal coherence.

Figure 4.5 illustrates the temporal coherence at a ship speed of 2 knots for various
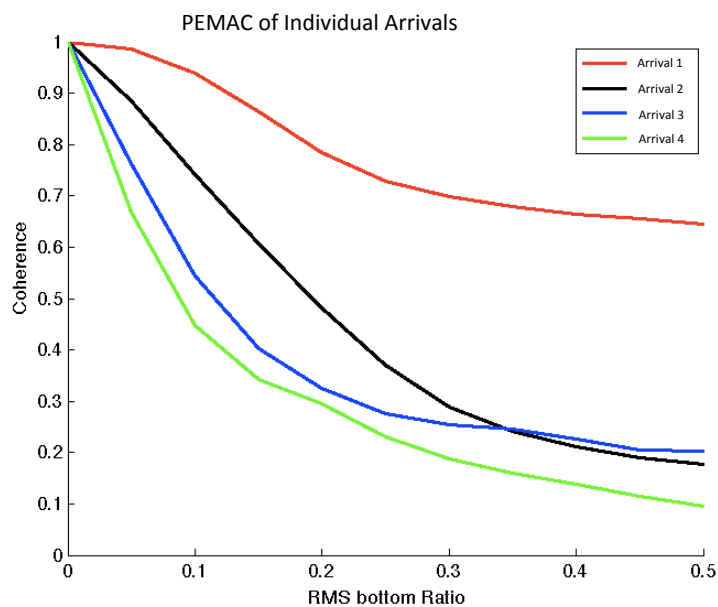
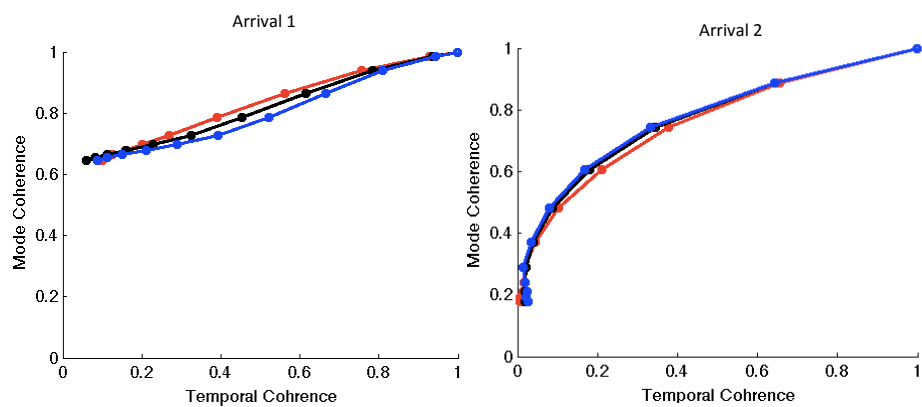**Figure 4.2:** PEMAC from a 100Hz signal at a range of 20km and a parallel tow path with a ship speed of 2kts.

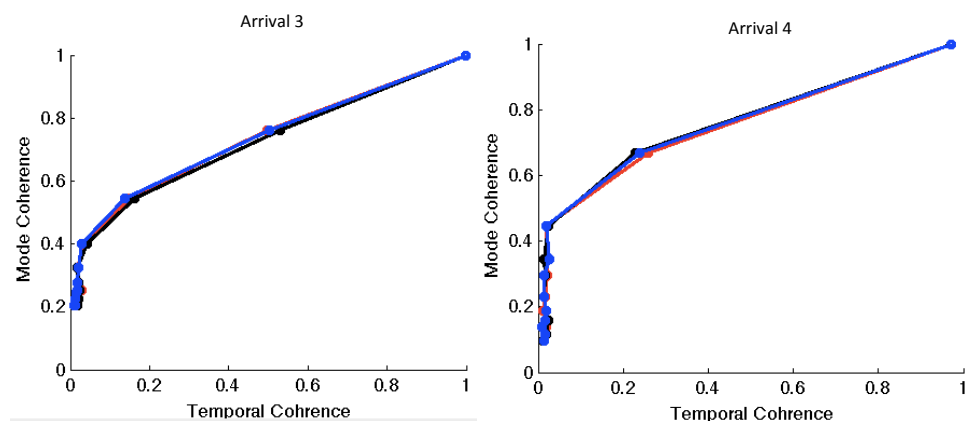**Figure 4.3:** PEMAC vs. Temporal Coherence for Arrivals 1 and 2

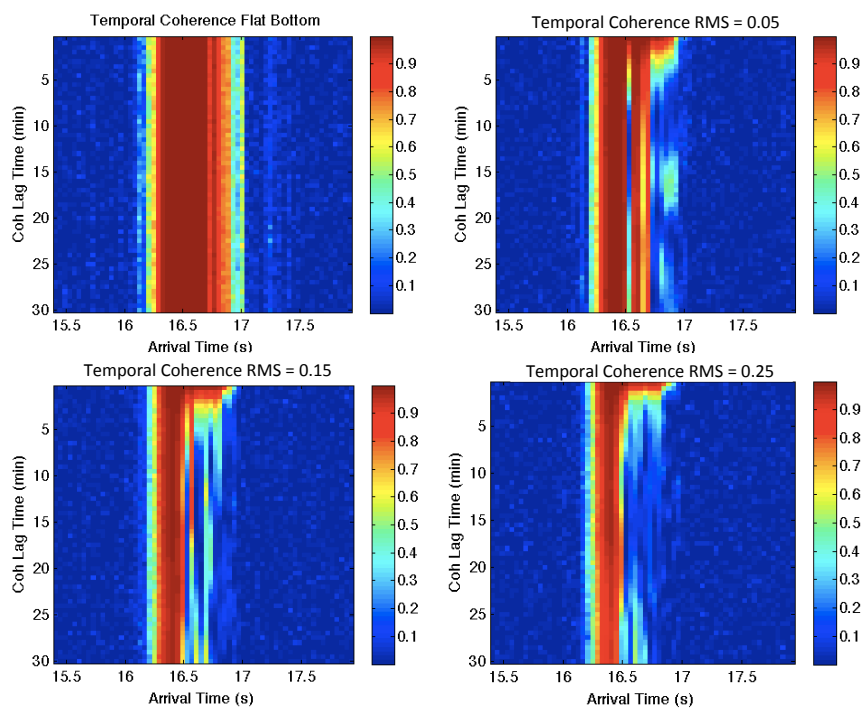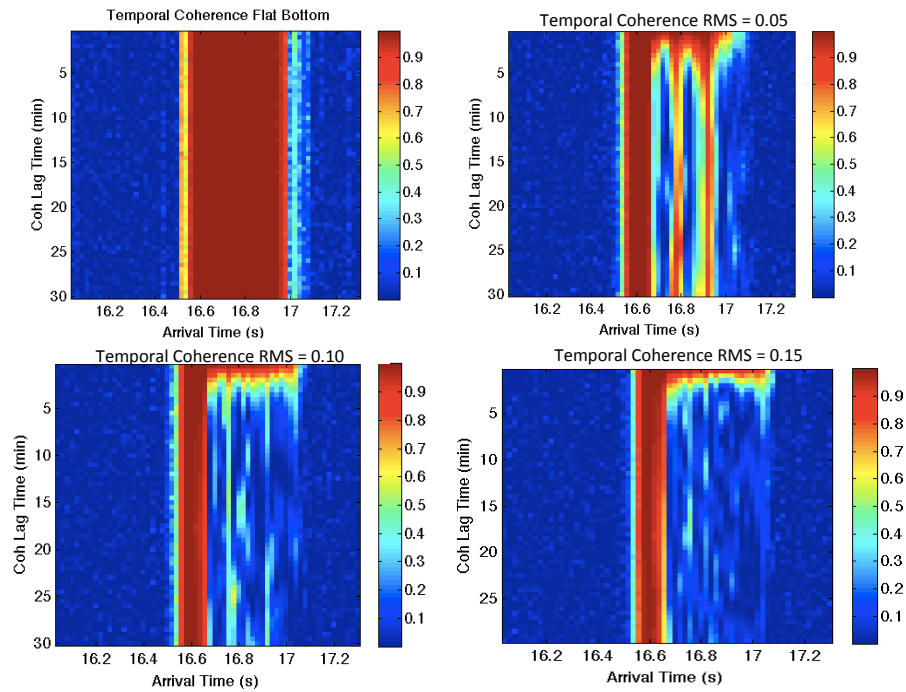**Figure 4.4:** PEMAC vs. Temporal Coherence for Arrivals 3 and 4

Figure 4.5: Temporal coherence from a 100Hz signal at a range of 25km and a tangential path with a ship speed of 2kts. Here the RMS bottom amplitude to acoustic wavelength is (clockwise from top left) Flat, .05, .15, and 0.25

Figure 4.6: Temporal coherence from a 200Hz signal at a range of 25km and a tangential path with a ship speed of 2kts. Here the RMS bottom amplitude to acoustic wavelength is (clockwise from top left) Flat, .05, .10, and 0.15

RMS bottom amplitudes at 100Hz and a range of 25km. There is a full 30 minutes of coherence with a flat bottom as is expected because the relative path of the signal is constant in time. However, arrival structure (as illustrated in section 3.1) becomes randomized and temporal coherence is quickly diminished as RMS bottom amplitude becomes even a small fraction of an acoustic wavelength. Temporal coherence is lost first for the higher order higher grazing angle modes while the first mode retains high coherence times. The results for a 200Hz tangential track are illustrated in Figure 4.6 and are consistent with the 100Hz case.

Figures 4.7 and 4.8 illustrate the temporal coherence for a radial track with a starting range of 10km and a speed of 2kts. There is some loss of temporal coherence

for the 200Hz flat bottom case, however this is from a Doppler like effect. As the ship moves outward from the source, the angle of the acoustic arrivals change, resulting in a phase shift. This is evident in all the radial path results. As with the tangential path, the earlier arrivals dominated by the lower order modes have a longer coherence time than the later arrivals dominated by the higher order modes. However, temporal coherence for the radial track and a given RMS bottom is higher than that for a corresponding RMS bottom tangential path. This holds at both 100Hz and 200Hz and is due to bottom correlation lengths. The correlation between the paths taken between two instances in time for the radial path will be higher than those of a tangential path due to the fact that the two signals traversing a radial will propagate over much of the same bathymetric variations while the signals traversing of the tangential paths will be transmitted over two entirely different paths.

The effects of ship speed on a tangential path are illustrated in Figure 4.9 for 100Hz at speeds of 0.5kts, 1kt and 3kts at a range of 25km. The influence of ship speed is clearly visible. While coherence times are diminished for all speeds, the rate of loss is greater for higher speeds. Coherence is not computed for speeds above 3kts as 2kts appears sufficient cutoff at which the loss of coherence becomes overwhelming to all arrivals except the first for even small bathymetric variations.
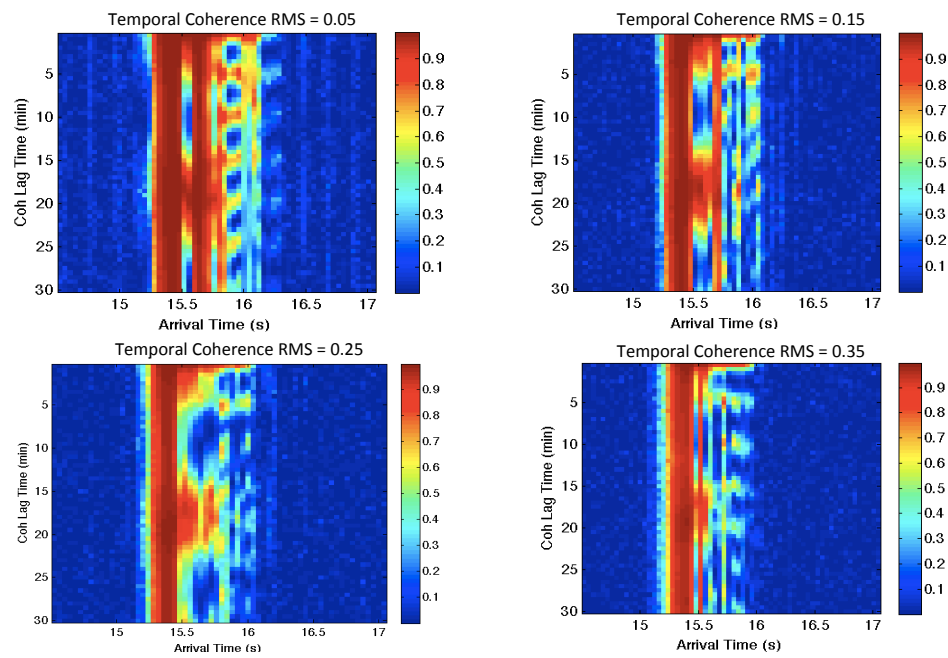
Figure 4.7: Temporal coherence from a 100Hz signal at a range of 25km and a radial path with a ship speed of 2kts. Here the RMS bottom amplitude to acoustic wavelength is (clockwise from top left) Flat, .05, .25, and .35
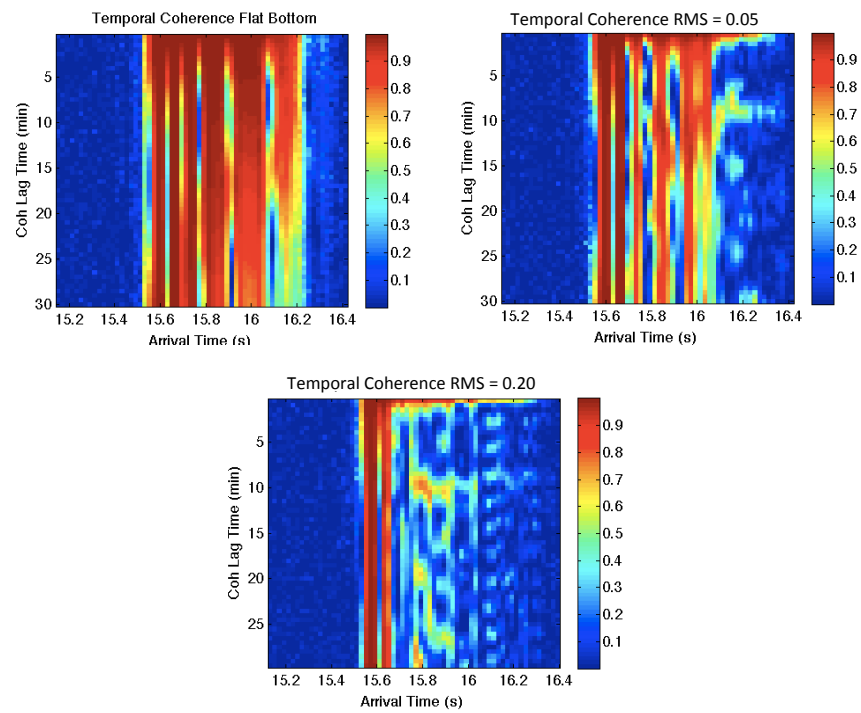
Figure 4.8: Temporal coherence from a 200Hz signal at a range of 25km and a radial path with a ship speed of 2kts. Here the RMS bottom amplitude to acoustic wavelength is (clockwise from top left) Flat, .05, and 0.2
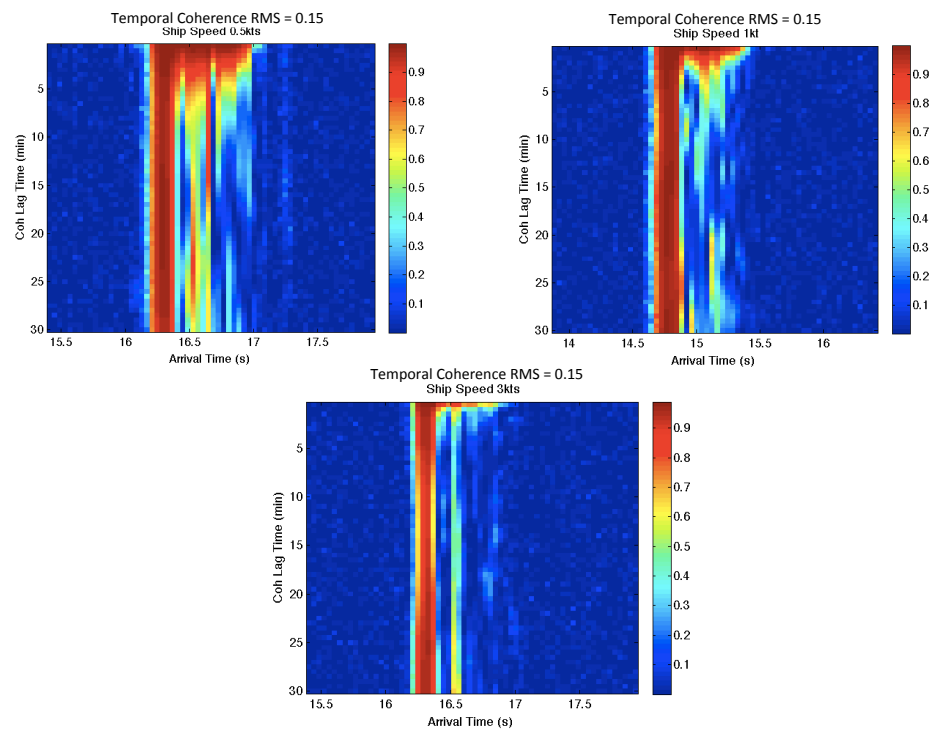
Figure 4.9: Temporal coherence from a 100Hz signal at a range of 25km a RMS bottom amplitude to acoustic wavelength ratio of .15. Here modeled tangential path ship speed is (clockwise from top left) 0.5kts, 1kt, and 3kts

Chapter 5
Fixed Platforms

The combined effects of bathymetric fluctuations and sound field variations are discussed in this chapter. The first scenario uses the large scale temporal fluctuations in the sound field as described in chapter 2. For each bathymetric realization the model is run for 1 hour worth of simulated temporal data with 30s intervals allowing for temporal coherence calculations of 30mins.

The temporal coherence results are illustrated in Figures 5.1 - 5.2. The mean depth is 80m, the range is 20km, and the hydrophone location of the temporal coherence calculation is chosen to be 45m. The results are not as expected based on previous chapters findings. The temporal coherence when a bottom is present is in some instances greater than or equal to that of a flat bottom. However, a simple explanation follows. Temporal coherence is lost in two ways, deterministic and random. In this instance the deterministic loss of coherence is caused by a slow shifting of modes across
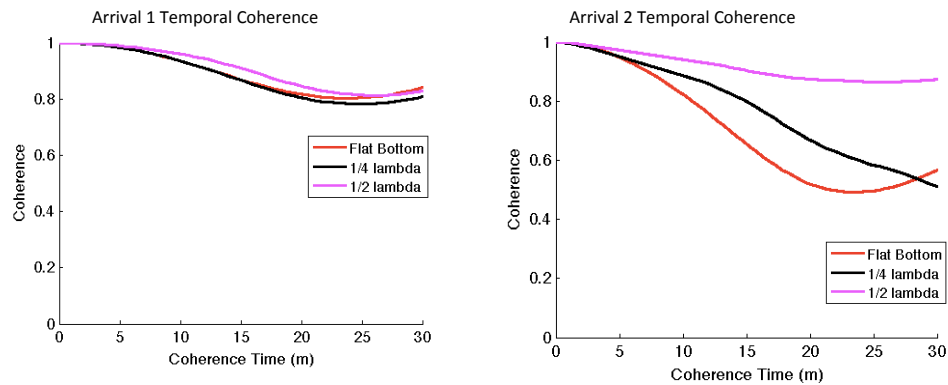
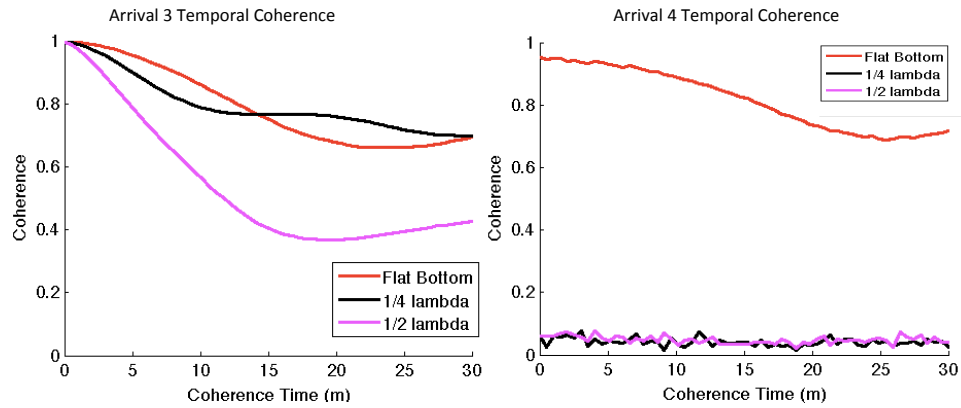**Figure 5.1:** Temporal Coherence for Arrivals 1 and 2

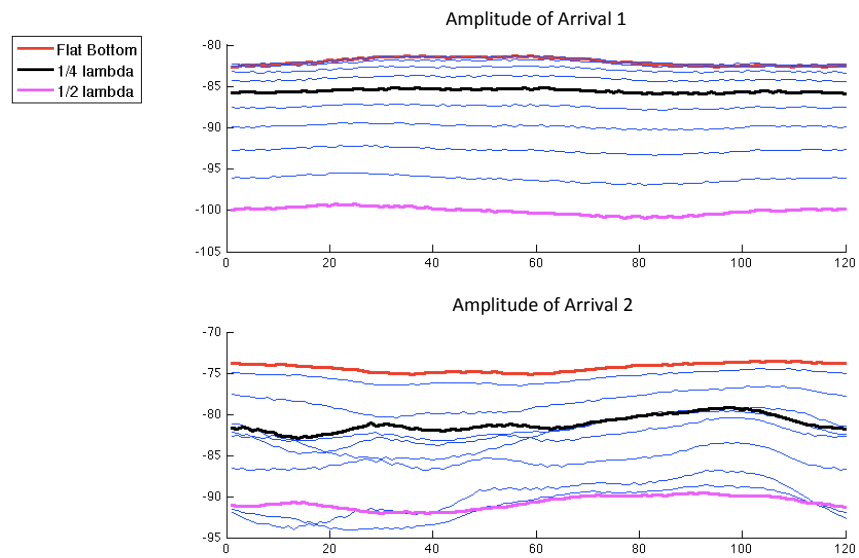**Figure 5.2:** Temporal Coherence for Arrivals 3 and 4

Figure 5.3: Amplitudes for Arrivals 1 and 2

the receiver location. A phase shift, that can be tracked and removed, is produced.

Figures 5.3 and 5.4 present the amplitude and phase for arrivals 1 and 2 respectively.

The amplitude of the flat bottom case remains relatively constant for both modes,

however a phase shift is apparent. This phase shift is simply subtracted out of the
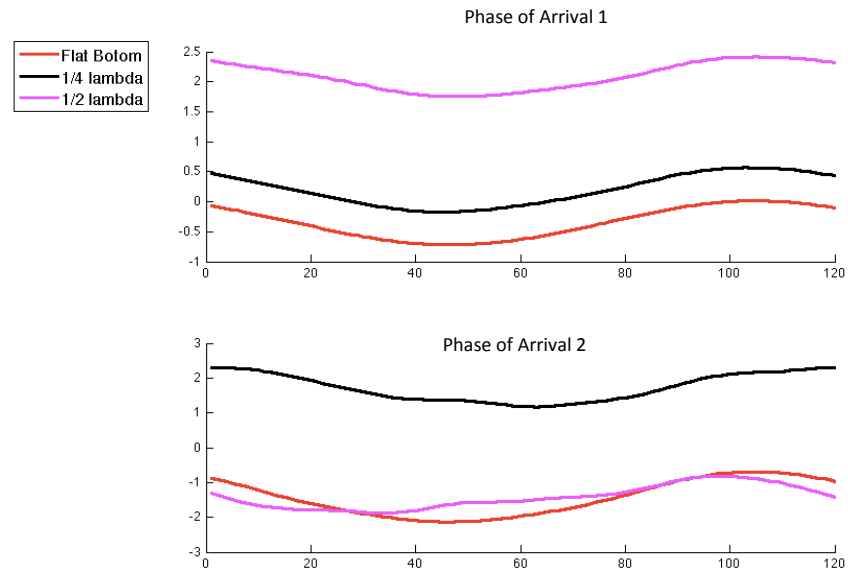
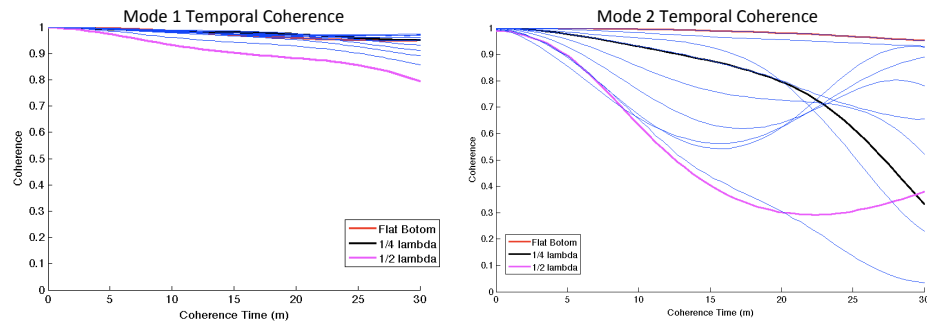**Figure 5.4:** Phase for Arrivals 1 and 2

Figure 5.5: Temporal Coherence for Arrivals 1 and 2 with the Deterministic Factor Removed

pulse response and the temporal coherence recomputed.

The temporal coherence results minus the deterministic part are illustrated in Figures 5.5 - Figure 5.6. The results are now consistent with expectations. The arrivals for the flat bottom case remain coherent over the entire calculation time. As
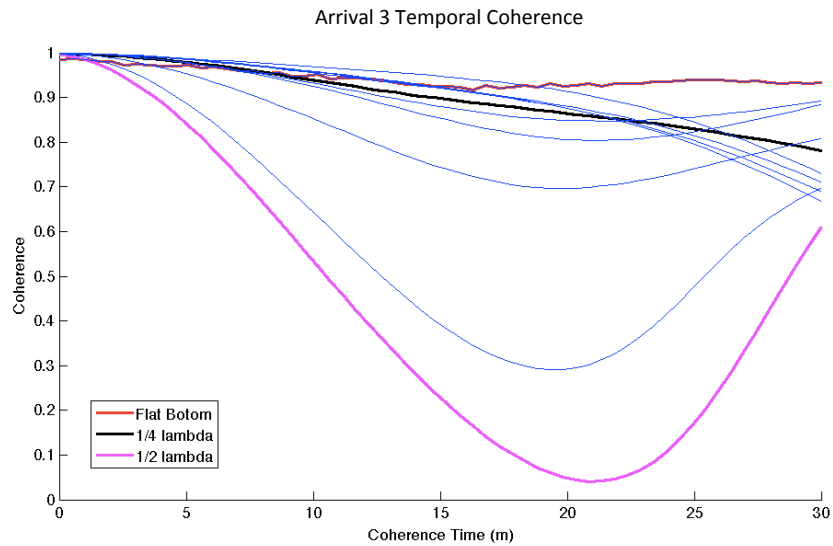
Figure 5.6: Temporal Coherence for Arrival 3 with the Deterministic Factor Removed

bottom RMS increase, coherence time decreases for each of the arrivals. This simple example illustrates that small changes in bottom bathymetry can have an impact on temporal coherence and is hypothesized to be due to the changing footprint of the acoustic path. The acoustic footprint is the location where the acoustic field interacts with the bottom. Small changes in the water column sound field can impact the acoustic , which as a result can change where and at what angle the sound interacts with the bottom. With large enough changes, the signal may vary enough that coherence is lost.

The second scenario combines the RMS bottom bathymetry fluctuations with the high frequency internal wave data as gathered by the SHARK array. For each RMS bottom realization, the model is run forward in time with a 2hr period of high internal wave activity with thermistor data from the SHARK array. Only one sound speed
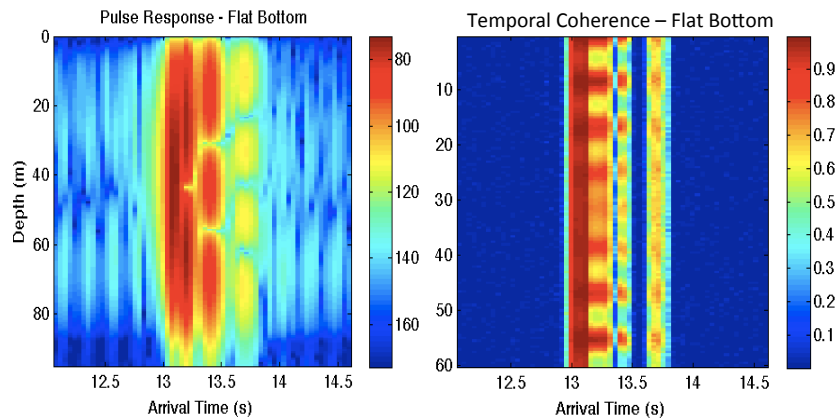
Figure 5.7: (Left) PE model prediction of Pulse response at 100Hz for a flat bottom bathymetry case (Right) Temporal Cohrence for an 100Hz signal with flat bottom bathymetry.

profile is used for the entire 20km range. This approximates an internal wave train traveling perpendicular to the acoustic travel path. The resolution of the SHARK data is every 30s and appears to be sufficient to resolve all the major variations in the sound speed. To begin the model is first run with only the internal wave fluctuations and no bathymetric fluctuations. Figures 5.7 and 5.8 present the pulse response and temporal coherence data for a 100Hz and 200Hz signal respectively with a flat bottom.

Figures 5.9 and 5.10 illustrate the temporal coherence including both internal wave and bathymetric variations for 100Hz and 200Hz. While the pulse response for each of these is not included in these figures, they are similar to those shown in Chapter 3. Mode structure becomes more randomized as the ratio of RMS bottom variation to acoustic wavelength increases and temporal coherence decreases for later order
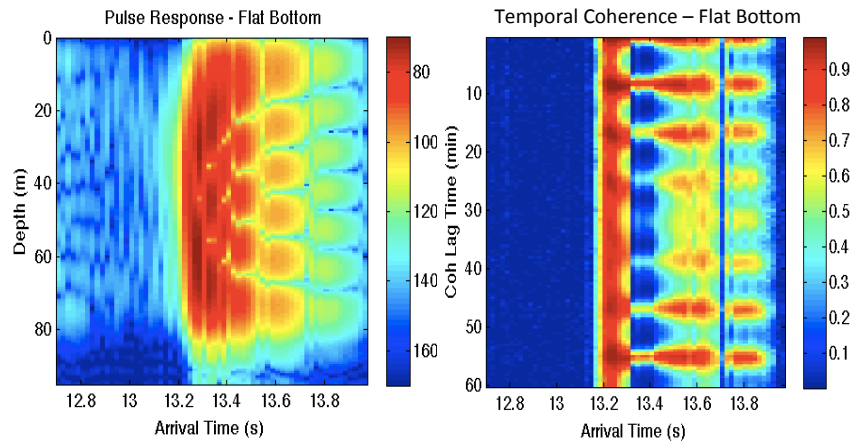
Figure 5.8: (Left) PE model prediction of Pulse response at 200Hz for a flat bottom bathymetry case (Right) Temporal Cohrence for an 200Hz signal with flat bottom bathymetry.
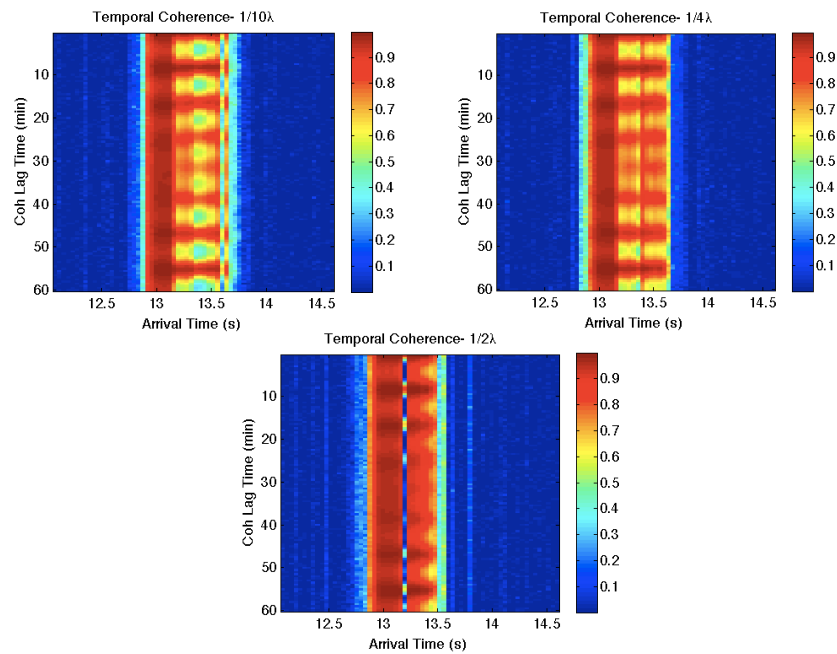

Figure 5.9: Temporal coherence for a 100Hz signal and a (Left top) $\frac{1}{10}\lambda$ RMS bottom, (Right top) $\frac{1}{4}\lambda$ RMS bottom, and (Bottom) a $\frac{1}{2}\lambda$ RMS bottom.

modes. The coherence time of the early modes appears to increase with increasing bathymetric variations, however this is just a result of a broadening of the first mode due to randomization.
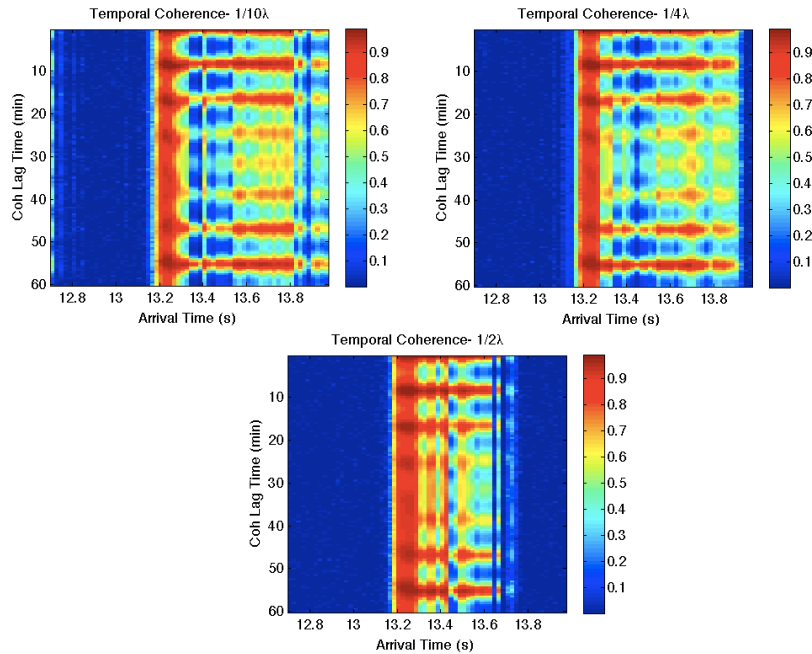

Figure 5.10: Temporal coherence for a 200Hz signal and a (Left top) $\frac{1}{10}\lambda$ RMS bottom, (Right top) $\frac{1}{4}\lambda$ RMS bottom, and (Bottom) a $\frac{1}{2}\lambda$ RMS bottom.

Next, the effects of small scale sound field fluctuations on PEMAC are examined. The wave height of the sound field fluctuation is increased in 1m increments and the PEMAC is calculated for each instance. Figures 5.11 and 5.12 presents the arrival structures and PEMAC data at 200Hz and 800Hz at a range of 10km. A 10km range is chosen due to modeling constraints and the ideal case is a two layer sound speed with no sinusoidal fluctuations present. At 200Hz there are relatively clean separable modes for all wave heights shown. As wave height increases, PEMAC is reduced slightly for the early arrivals, however the late arrivals retain PEMAC . The 800Hz data produces a more diverse picture. Mode structure becomes distorted for
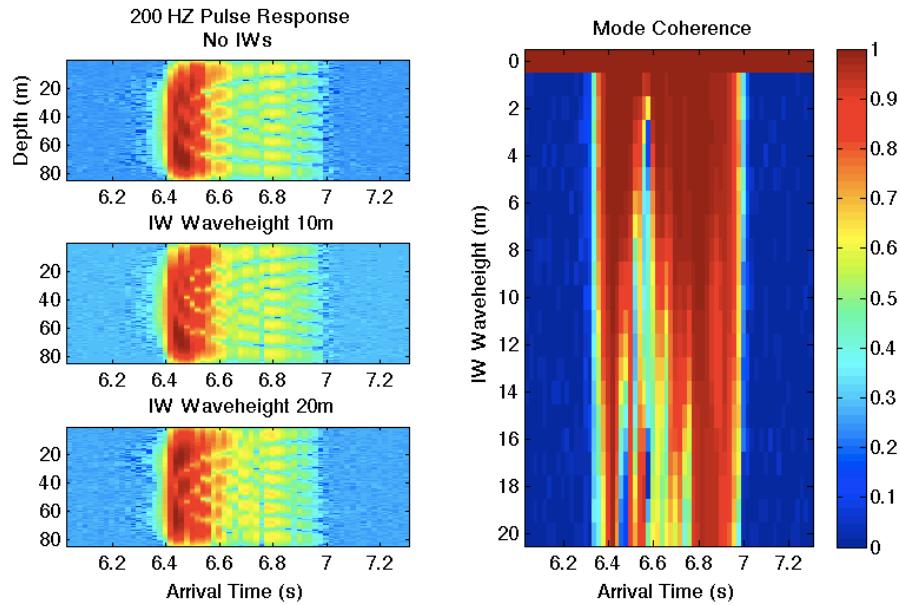
Figure 5.11: Pulse response and PEMAC for a 200Hz signal at a range of 10km

the earlier arrivals and PEMAC is reduced or entirely lost. However, the higher order modes retain coherence and structure. In both cases presented, the retention of higher order PEMAC is attributed to high angle of incidence with which the acoustic field travels through the sound field fluctuations.

When the sound field fluctuations are converted from wave height in meters to a ratio with the acoustic wavelength, $\frac{h}{\lambda}$, clear comparisons can be made with bathymetric fluctuations. When $\frac{h}{\lambda} = 1$, PEMAC remains stable over all modal arrivals. At a ratio of 2.5 early order arrivals begin to lose coherence and by a ratio of 4-5 only the later arrivals retain PEMAC. This is in remarked difference to the bottom bathymetry results which only require a ratio of $\frac{1}{4}$ to $\frac{1}{2}$ for PEMAC to be lost for all except the first arrival and later arrivals lose coherence first.
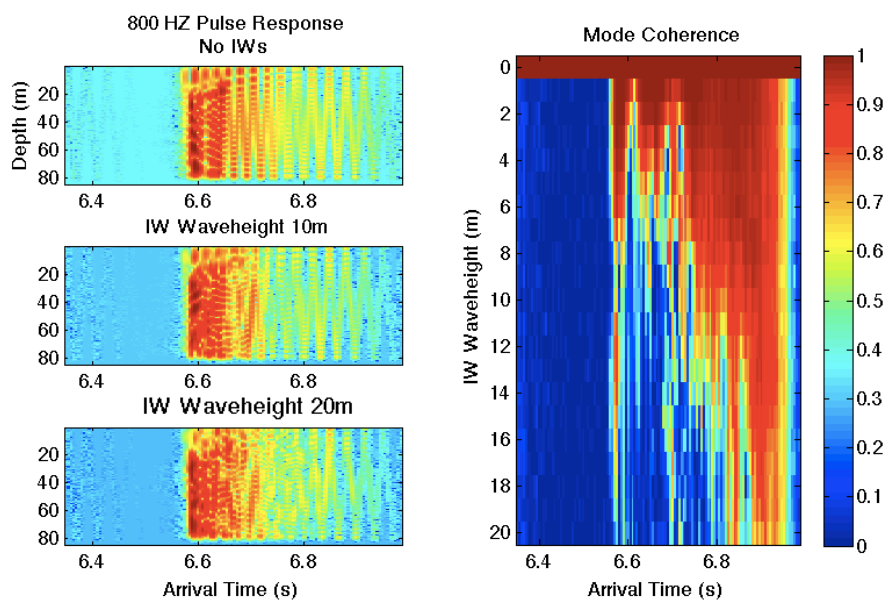
Figure 5.12: Pulse response and PEMAC for a 800Hz signal at a range of 10km

Chapter 6
Conclusions

It has been shown that bottom bathymetry can have a noticeable impact on both modal arrival structure and temporal coherence. In fact it is a strong first order effect. A PEMAC calculation has been introduced to estimate the effect of bathymetric fluctuations on PE mode structure. When PECM is high, the PE modal arrival structure of the acoustic signal remains stable with clear separable modes. As PEMAC decreases, arrival structure becomes randomized. Higher order modes are effected before lower order modes.

PEMAC was also computed when short scale water column fluctuations were present. Lower order modes were more greatly effected than higher order modes. However, overall the arrival structure remains more robust towards water column fluctuations than bathymetric fluctuations. A water column fluctuation must be on the order of 10 times greater than a bathymetric fluctuation in order to produce a similar effect in loss of PEMAC.

When PEMAC is high, the acoustic signal is robust and large scale water column fluctuations only translate the modes past the receiver and result in a deterministic loss of temporal coherence after a long time scale. When PEMAC is low, the acoustic signal is unstable and any small temporal changes in the water column result in a loss of temporal coherence. Higher order, higher grazing angle modes are affected first. This is most noticeable when bathymetric variations are on order of $\frac{1}{4}$ of an acoustic wavelength. When fluctuations near or exceed $\frac{1}{2}$ an acoustic wavelength, modal arrivals become completely randomized and any usable coherence is lost beyond

the first mode.

Additionally, mobile platforms and fixed platforms present inherent differences with regards to signal processing and temporal coherence. Coherence is primarily lost through bottom effects and water column fluctuations on a fixed platform. Since the propagation path is constant, this makes fixed platforms ideal from which to study the impact of internal waves on temporal coherence. Mobile platforms inherently lose coherence due to motion of the ship traversing over bathymetric variations. As ship speed increases, the loss of coherence also increases and, by a speed of 2 knots, coherence loss is equal to that from a high energy internal wave. Adding in small scale internal wave variations along the path of a moving ship would not change the conclusions, as coherence will decorrelate quicker from the ship motion.

While the modeled cases presented in this dissertation are idealized, the results are similar to the those from the SW06 experiment. At low frequencies, when bottom fluctuations are likely to be a small fraction of acoustic wavelength (i.e. $< =100$Hz), the predominate first order effect would result from internal waves. At mid frequencies, both internal waves and bottom variations would have an effect, with high order modes more prominently affected by the bottom and low order modes most prominently affected by sound field fluctuations. At high frequencies ($> =800$Hz), only a small, long-scale variation in bottom bathymetry (on the scale of a meter or less) would be needed to reduce coherence beyond a usable scale. Only the remaining first arrival would retain usable coherence information from the sound field fluctuations.

In brief, by including both bathymetric variations and internal wave fluctuations in modeling work to study the loss of temporal coherence, a more complete and consistent analysis occurs with results being comparable to those from the SW06 experiment.

References

[1] H.A. Deferrari, "Temporal coherence of mode arrivals," J. Acoust. Soc. Am. **124**, EL104–EL109 (2008).

[2] H.A. DeFerrari, Observations of low-frequency temporal and spatial coherence in shallow water, J. Acoust. Soc. Am. **125**, EL45-EL49 (2008).

[3] Yang, T. C. "Measurements of temporal coherence of sound transmissions through shallow water." The Journal of the Acoustical Society of America 120 (2006).

[4] F. Dyson, W.H. Munk, and B. Zetler, "Interpretation of multipath scintillations Eleuthera to Bermuda in terms of internal waves and tides," J. Acoust. Soc. Am. **59**, 1121-33 (1976).

[5] W.H. Munk, "Sound channel in an exponential stratified ocean, with applications to SOFAR," J. Acoust. Soc. Am. **55**, 220-6 (1974).

[6] S. McDaniel and D McCammon, "Mode coupling and the environmental sensitivity of shallow-water propagation loss predictions," J. Acoust. Soc. Am. **82**, 217–223 (1987).

[7] J.C. Preisig and T.F. Duda, "Coupled acoustic mode propagation through continental shelf internal solitary waves,"IEEE J. Ocean Eng. **22**, 256–269 (1997).

[8] T.F. Duda and J.C. Preisig, "A modeling study of acoustic propagation through moving shallow water solitary wave packets," IEEE J. Ocean Eng. **24**, 16–32 (1999).

[9] K.B. Smith, Convergence, stability, and variability of shallow water acoustic predictions using a split-step Fourier parabolic equation model, J. Comp. Acoust., **9**, No. 1, pp. 243-285 (2001).

[10] Palmer, D. R., et al. "Ray path identification and acoustic tomography in the Straits of Florida." Journal of Geophysical Research: Oceans (19782012) 90.C3 (1985): 4977-4989.

[11] Palmer, D. R., T. M. Georges, and R. M. Jones. "Classical chaos and the sensitivity of the acoustic field to small-scale ocean structure." Computer Physics Communications 65.1 (1991): 219-223.

[12] Creamer, Dennis B. "Scintillating shallow?water waveguides." The Journal of the Acoustical Society of America 99 (1996): 2825.

[13] Dozier, L. B., and F. D. Tappert. "Statistics of normal mode amplitudes in a random ocean. I. Theory." The journal of the Acoustical Society of America 63 (1978): 353.

[14] Dozier, Lewis B. "Numerical solution of coupled mode equations for rough surface scattering." The Journal of the Acoustical Society of America 73 (1983): S96.

[15] Young, A. C. Two dimensional acoustic propagation through oceanic internal solitary waves: Weak scattering theory and numerical simulation, Masters of Science Thesis, Department of Oceanography, Naval Postgraduate School, Monterey, CA (2006).

[16] Colosi, John A., and Andrey K. Morozov. "Statistics of normal mode amplitudes in an ocean with random sound-speed perturbations: Cross-mode coherence and mean intensity." The Journal of the Acoustical Society of America 126 (2009): 1026.

[17] Rouseff, Daniel, et al. "Mid-frequency sound propagation through internal waves at short range with synoptic oceanographic observations." The Journal of the Acoustical Society of America 124.3 (2008): EL73-EL77.

[18] Williams Jr, A. O. "Mode interactions in an isovelocity ocean of uniformly varying depth." The Journal of the Acoustical Society of America 67 (1980): 177.

[19] Fortuin, Leonard. A survey of literature on reflection and scattering of sound waves at the sea surface. No. SACLANTCEN-TR-138. Saclant ASW Research Centre La Spezia (Italy), 1969.

[20] Roderick, William I., and Benjamin F. Cron. "Frequency spectra of forward scattered sound from the ocean surface." The Journal of the Acoustical Society of America 48 (1970): 759.

[21] Parkins, B. E. "Reflection and scattering from a time varying rough surfacethe nearly complete Lloyd's Mirror effect." The Journal of the Acoustical Society of America 49 (1971): 1484.

[22] Mitchell, Stephen K., and Fredrich W. Machell. "Observations of low frequency acoustic interaction with the ocean surface." The Journal of the Acoustical Society of America 86 (1989): 1118.

[23] Brown, M. Vertner, and George V. Frisk. "Frequency smearing of sound forward scattered from the ocean surface." The Journal of the Acoustical Society of America 55 (1974): 744.

[24] Roderick, William I., and Roy L. Deavenport. "Doppler characteristics of sea surface reflected and scattered acoustic signals induced by surface wave motion." OCEANS'93. Engineering in Harmony with Ocean. Proceedings. IEEE, 1993.

[25] Jensen, F.B., 2000: Computational Ocean Acoustics. Springer, New York, NY, 229 pp

[26] Tappert, Fred D. "The parabolic approximation method." Wave propagation and underwater acoustics. Springer Berlin Heidelberg, 1977. 224-287.

[27] Smith, Kevin B., and Frederick D. Tappert. UMPE: The University of Miami Parabolic Equation Model. Version 1.0. No. MPL-U-27/93. Scripps Institution of Oceanography La Jolla Ca Marin Physical Lab, 1993.

[28] Smith, Amy R., and Kevin B. Smith. "Mode functions for the wide-angle approximation to the parabolic equation." The Journal of the Acoustical Society of America 103 (1998): 814.

[29] J. Geoff, "3-D interpolation of subsurface stratigraphic architecture in the vicinity of the SW06 region based on interpreted chirp seismic reflection data. Univ. Texas, Austin. Sheraton Hotel, Fort Lauderdale, Fl. Feb 2008. Presentation.

[30] McDaniel, Suzanne T. "Mode coupling due to interaction with the seabed." The Journal of the Acoustical Society of America 72 (1982): 916.

[31] Evans, R. B. "A coupled mode solution for acoustic propagation in a waveguide with stepwise depth variations of a penetrable bottom." The Journal of the Acoustical Society of America 74 (1983): 188.

[32] A.E. Gill, Atmosphere-Ocean Dynamics. Academic Press, London, United Kingdom, 661 pp. (1982).

[33] Shroyer, Emily L., James N. Moum, and Jonathan D. Nash. "Nonlinear internal waves over New Jersey's continental shelf." Journal of Geophysical Research: Oceans (19782012) 116.C3 (2011).